ALGORITHM THEORETICAL BASIS DOCUMENT

ATBD 2.15

Atmospheric corrections over land

Richard Santer, Véronique Carrère, David Dessailly, Philippe Dubuisson, and Jean-Claude Roger

Laboratoire Interdisciplinaire des Sciences de l'Environnement
(LISE)
Université du Littoral-Côte d'Opale, Wimereux, France

Table Of Contents

List Of Figures

1. Introduction

One of the MERIS products at Level 2 will be the reflectances in 13 MERIS bands corrected for gaseous absorption and Rayleigh scattering. Although the MERIS instrument will have 15 programmable channels available (a limitation due to transmission capacity), reflectances will only be derived from the 13 bands which are not strongly contaminated by atmospheric gaseous absorptions. The two contaminated channels (namelly the 760 nm channel for O_2 and the 900 nm channel for water vapour) will be devoted to the retrieval of gaseous abondances and therefore cannot be used to get surface reflectance. The correction of surface reflectance for aerosols, are deferred to Level 3 processing.

This document provides a description of the different stages followed to achieve surface reflectance retrieval. The algorithm has been developed under the following restrictions: (1) to find the best compromise between the quality of the results and the operational requirements, (2) to use an instrument initially devoted to oceanographic applications for atmospheric correction over land (no infrared channels, ...), and (3) to account for initial ESA requirements such as the impossibility of using information derived from other ENVISAT instruments in real time for atmospheric corrections or any kind of database (such as elevation maps) in the algorithm. This algorithm takes advantage of constraints in MERIS observational geometry: the instrument observation is limited to a 68.5 degrees FOV and solar illumination angles are between 0 and 80 degrees due to orbital geometry and data acquisition capabilities. Therefore extreme geometries where sources of uncertainty are the strongest are mainly avoided. As for constraints due to MERIS spatial resolution (300 m for the Full Resolution mode, up to 20 minutes per orbit, and 1200 m for the Reduced Resolution mode which is continuously recorded), the issue of adjacency effects and directional effects is assessed in separate documents as part of the sensitivity and algorithm validation analysis and will only be mentioned here.

A first classification of the top of atmosphere radiances over land (identified from geographical informations) is performed at Level 1b. The land process at Level 2 begins with pixel re-classification: discrimination between water and land along the coast line, identification of inland waters. Then among the pixel classified as bright after Level 1, we will separate clouds and bright land surfaces based on altitude and spectral dependency. This pixel "reclassification" stage is discribed in the ATBD on Pixel Identification (ATBD 2.17). A general flow chart including Pixel Identification and the different steps of the Atmospheric Correction Algorithm is presented in Figure 1.

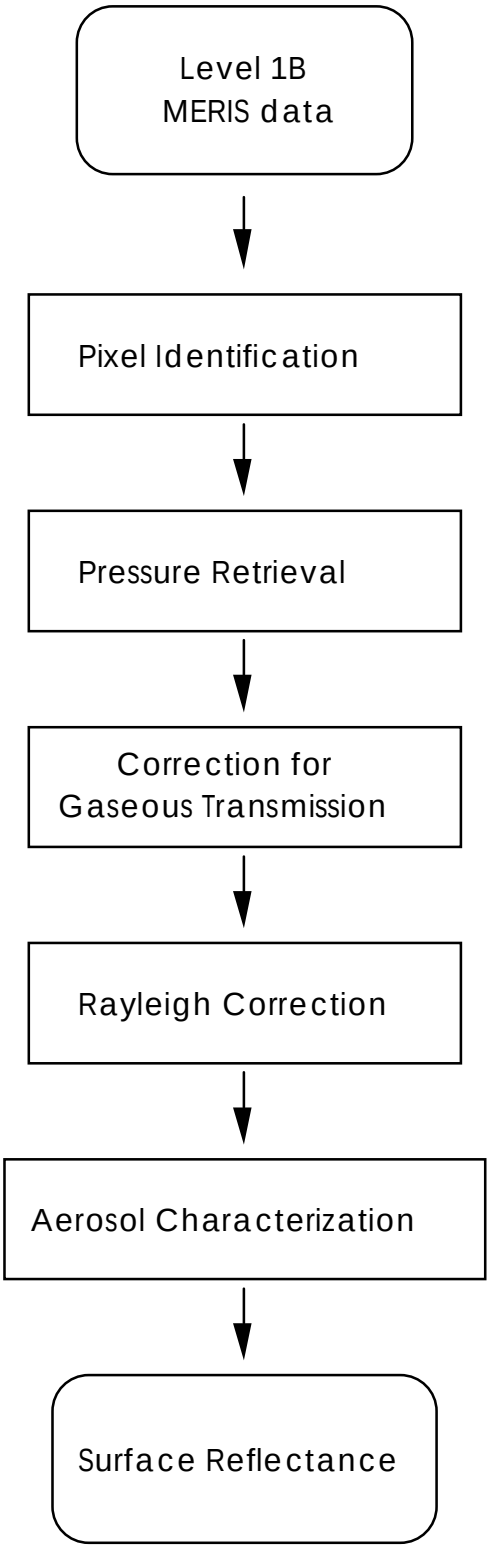

Figure 1: General flow chart of the surface reflectance retrieval scheme, to be applied to a 32 x 64 pixel window.

A preliminary stage to an atmospheric correction scheme is to have a simple, but robust, modeling of the signal which allows to simply convert the TOA radiance into surface reflectance. The signal decomposition involves three steps. In a first stage, the gaseous absorption is removed from the signal. The well-known ozone correction is based on ECMWF data. For the water vapour absorption, a differential method between 900 and 890 nm is currently proposed to derive the water vapour content. We skip this retrieval by directly associating the ratio of the radiances at 900 and 890 nm to the water vapour transmittance in any other MERIS bands. In doing so, we cancel systematic errors affecting the water vapour absorption such as the coupling between aerosol scattering and gaseous absorption. The same technique is applied for the O_2 transmittance by associating the O_2 transmittance at 760 to the ratio 760/753.75 nm . Simulations which include the coupling between absorption and scattering indicate that this direct association is more accurate than a computation which involves O_2 or H_2O concentration as inputs.

IMPORTANT NOTE

Correction for gaseous absorption is applied above water pixels, prior to the turbid pixel detection (see ATBD 2.5), as well as above land.

We then correct for Rayleigh scattering. Computations with the successive orders of scattering code indicated that we can use a schematic vertical structure of the atmosphere with a pure molecular layer above the aerosols and keep a good accuracy. The signal is then decomposed to convert the TOA radiance into a top of aerosol radiance. We also propose simple and reduced look-up tables (LUTs) to correct Rayleigh primary scattering from multiple scattering and a simple formulation for Rayleigh transmittance.

The Rayleigh contribution depends on the barometric pressure. This pressure is determined using two MERIS bands at 760 and 753.75 nm in a differential method using the O_2 transmittance which only depends on the product air mass times pressure square. A simple correction for the coupling between scattering and absorption versus the surface reflectance is proposed. This surface pressure retrieval is shown to have a better accuracy compared to ECMWF data associated to digital map to correct for surface elevation.

The correction for the aerosols is primarily based on standard aerosols models (here the 12 models used for POLDER aerosol remote sensing over land). Then a reference to the aerosol climatology is done to set the refractive index. The remaining, aerosol optical thickness and the slope

of the Junge size distribution, are determined from specific observations over dense dark vegetation (DDV).

DDV pixels are detected using a spectral index, the Atmospheric Resistant Vegetation Index, ARVI, (Kaufman and Tanré, 1992). Standard values for DDV reflectances at 412, 443 and 665 nm are proposed in order to retrieve the MERIS reflectances by the proper aerosol model. Of course this aerosol retrieval is only possible over DDV pixels which leads to define a MERIS window for which the same aerosol model applies. Within a window, we then need to weight the different informations about the aerosol resulting from pure land observations as well as for mixed windows including coastal water and land. We will also report on the criteria used to make a choice between our aerosol retrieval and a backup based on the aerosol climatology available as auxiliary parameter.

IMPORTANT NOTE

In the operational MERIS Level 2 processing, the averaging of aerosol properties over a 32x64 window described below is not performed. The atmospheric corrected reflectance Level 2 product is therefore the reflectance corrected for gaseous absorption and Rayleigh scattering, in 13 MERIS bands. Aerosol parameters: optical thickness and epsilon $\left(\varepsilon(775,865) = \frac{\rho_a(775)}{\rho_a(865)} \right)$, are computed above DDV pixels. The interpolation of aerosol fields applicable to all land pixels, from the Level 2 product, and the correction of surface reflectance for aerosols, are deferred to Level 3 processing.

2. Algorithm overview

2.1. Objectives

The first objective is to provide surface reflectances for all of the MERIS bands, except for those which are specifically devoted to the retrieval of gaseous abundance: the two bands for O_2 (at 760 and 765 nm) and the water vapour band at 900 nm. We propose to use surface reflectance instead of radiance because of its more geophysical significance. This conversion of the measured radiance into reflectance is only valid for horizontal targets for which we know the incident solar zenith angle. This means that for non-flat areas, a pixel by pixel correction is needed based on a knowledge of the terrain slope which is not available at present time on an operational basis.

Because the correction for the aerosol is questionable, we wish to provide the user with an easy way to retrieve the reflectance above the surface+aerosol system from available attached information. This information can be a starting point to develop spectral indices for land classification. Information required for the algorithm will also be attached as a product: surface pressure, aerosol type and abundance.

Non Lambertian and adjacency effects are not taken into account in the corrections as described here. Accounting for BRDF in the atmospheric correction scheme is presented in a separate ATBD (ATBD 2.19). As for adjacency effects, no simple but accurate correction is presently available. First order corrections for adjacency effects are the subject of a separate ATBD (ATBD 2.21), yet not implemented in the MERIS operational processor.

A validation plan, described in a separate document, will allow some additional tests: (1) MERIS products could be validated through comparison with other independent sources, such as MODIS, POLDER, etc.; (2) validity of the vertical structure and spectral stability will be tested. Although the use of an aerosol climatology database, derived from extensive sunphotometer networks could be essential to validate the algorithm at a local scale, we do not see it fit for an operational environment at a global scale.

2.2. Principle of atmospheric correction

The photons which enter the sensor have different origins and a 6S-like signal decomposition is proposed (Vermote et al., 1995) in an attempt to formulate the different contributions in the simplest way:

(i) the Rayleigh scattering,

(ii) the aerosol scattering,

(iii) the absorption by gases,

(iv) the contribution of the surface, which depends directly on its reflectance which is the useful component.

It has to be pointed out at this stage that several members of the Université du Littoral-Côte d'Opale group have directly contributed to the development of the 5S and 6S codes and are therefore very familiar with them. The 5S and 6S formulations are very different: the 6S code includes multiple scattering (Successive Order of Scattering method) instead of the classical linear formulation. Moreover, the methodology used in the present algorithm is very different from the 5S formulation: the atmosphere is decomposed into two decoupled layers (aerosol + Rayleigh) while 5S and 6S approaches rely on multiple layers.

This signal decomposition is primarily applied to the top of atmosphere (TOA) radiance based on runs of radiative transfer codes. These runs involve each of the specific contributors in order to model them and so that coupling between two of them becomes more explicit. The formulation of the signal is a simple analytical formula involving each contribution, allowing a straight forward inversion of the signal to retrieve the surface reflectance.

3. Algorithm description

3.1. Theoretical description

3.1.1. Conditions for simulating the ocean - land system

Because the gaseous absorption is quite residual in the MERIS bands to which we apply the atmospheric correction, we can start by describing the conditions necessary to compute the atmospheric diffusion:

(i) The radiation field is described by four components. Because the ellipticity of light vibration for the terrestrial atmosphere-surface system is assumed to be on average equal to zero, we can describe the radiation field by three Stokes parameters only: I, Q, U. It is pointed out that through the multiple scattering, it is necessary to account for the polarization in the computation of the total radiance.

(ii) The phase matrix for the Rayleigh is quite well established if we neglect the asymmetry of the molecules.

The Rayleigh phase function is expressed as follows:

$$P(\Theta) = \frac{3\,A\,(1 + cos^2(\Theta))}{4} + B \qquad (01)$$

where A = 0.9587256 and B = 0.0412744 are given in the 6S manual (Vermote et al., 1995) to account for the molecule asymmetry. The scattering angle Θ is expressed as:

$$cos(\Theta) = sin(\theta_s)sin(\theta_v)cos(\varphi) - \mu_s\,\mu_v \qquad (02)$$

where subscripts *s* and *v* stand for solar and view, θ is the zenith angle, φ the difference in azimuth (with φ = 180 in the backscattering region according to the S.O. convention) and μ is the cosine of the zenith angle. The Rayleigh optical thickness versus wavelength is known at a standard pressure of 1013 hPa. This optical thickness is proportional to the barometric pressure at the surface.

(iii) The aerosols are supposed to be spherical to apply the Mie theory. Moreover, one aerosol model corresponds to a single component (same equivalent refractive index) for the whole size spectrum.

(iv) Except during strong volcanic aerosol contamination, aerosols are mainly located in the lower troposphere while most of the molecules are above the aerosol layer. Then a simple description for the vertical distribution of the optical thickness δ is given by:

$$\delta(z) = \delta(0)\, e^{-z/H} \qquad (03)$$

where the scale height H is 2 km for the aerosols. The same schematic distribution is used for the Rayleigh but with H = 8 km. Only one aerosol model is considered for the whole atmospheric column.

(v) The spectral response function of the MERIS bands is accounted for in the computations of the basic Rayleigh optical thickness.

General information on MERIS bands is given in Table 1. Most of the MERIS bands have to be corrected for ozone absorption. The water vapour continuum has a significant contribution except in the blue. For oxygen, only the MERIS band for surface observation at 775 nm is slightly affected, but if we shift the lower wavelength by 6 nm, the transmittance is almost 1. So we recommend reducing the bandwidth to 10 nm between 774 nm and 784 nm to avoid doing this correction.

For the surface, the reflection is lambertian and we neglect the influence of the surroundings. As mentioned above, correction for directional effects involves knowledge of the surface BRDF which is a Level 3 MERIS product, not available for operational Level 2 data processing. The introduction of the environment effect is theoretically feasible but will lead to substantial computer time to correct for a second order effect. A first order correction is under investigation and will be described in a separate document.

Band #	center (nm)	δ_{O_3}	δ_R	Absorbers	T_{O_3}	T_{H_2O} line	T_{H_2O} line + cont.	T_{O_2}
1	412.0	0.000	0.320	----	1.	1.	1.	1.
2	442.0	0.003	0.239	O_3	0.998	1.	1.	1.
3	490.0	0.019	0.157	O_3	0.985	1.	1.	1.
4	510.0	0.039	0.133	O_3+H_2O	0.970	0.993	0.987	1.
5	560.0	0.100	0.091	O_3+H_2O^*	0.926	1.	0.992	1.
6	620.0	0.106	0.060	O_3+H_2O^*	0.922	1.	0.988	1.
7	665.0	0.049	0.045	O_3+H_2O	0.963	0.995	0.981	1.
8	681.0	0.034	0.041	O_3+H_2O	0.974	0.998	0.982	1.
9	705.0	0.020	0.036	O_3+H_2O	0.985	0.906	0.888	1.
10	753.75	0.009	0.027	O_3+H_2O^*	0.993	1.	0.978	1.
11	760.0	0.007	0.026	O_3+H_2O^*+O_2	0.994	1.	0.978	0.380
11b	765.0	0.006	0.025	O_3+H_2O^*+O_2	0.996	1.	0.978	0.648
12	775.0	0.000	0.024	H_2O^*+O_2	1.	1.	0.977	0.994
13	865.0	0.000	0.016	H_2O^*	1.	1.	0.970	1.
14	890.0	0.000	0.014	H_2O	1.	0.945	0.911	1.
15	900.0	0.000	0.013	H_2O	1.	0.647	0.601	1.

* only H_2O continuum absorption

Table 1: General informations about MERIS: Rayleigh optical thicknesses for a barometric pressure of 1013 hPa, Ozone optical thickness for 1 cm-atm of Ozone, composition of the absorbers in the different bands. For a solar zenith angle of 45 deg. and a nadir view, we also report the gaseous transmittance for the mid-latitude summer model according to GAME and 6S runs.

The computations will be conducted with the successive orders of scattering method (SOS, see Deuzé et al., 1989) which solves the transfer equation in a plane parallel atmosphere. Because of the medium size of the MERIS F.O.V. as well as a solar zenith angle limited to 80 degrees, we do not have to account for the Earth sphericity in the computations.

To account for the coupling between absorption and scattering, the MERIS reflectances have been simulated from GAME (Global Atmospheric ModEl), a radiative transfer model developed at the LOA (Laboratoire d'Optique Atmosphérique, Université des Sciences et Technologies de Lille, France) including (1) molecular, aerosols and clouds scattering and (2) H_2O, CO_2, O_3 and O_2 absorption. In this model, the absorption coefficients are obtained from line-by-line calculations (STRANSAC model, Scott, 1974; Dubuisson et al., 1996), using the HITRAN database (Rothman et al., 1992) and with a resolution of 10 cm^{-1} (about 0.5 nm for the O_2 absorption band). Water vapour absorption continuum (CKD 2.2 parametrization, Clough and al., 1992) is also included. Interactions between molecular absorption and scattering are accurately treated using the Discrete Ordinate Method (Stamnes et al., 1988) and the correlated k-distribution method (Lacis and Oinas, 1991).

Comparisons between GAME and reference calculations have shown differences less than or on the order of 2% and 4% in satellite radiances, respectively for water vapour and oxygen absorption, both for clear or cloudy atmospheres. These reference calculations consist of multiple scattering calculations at each step of a line-by-line model.

3.1.2. Signal decomposition

a) Removing gaseous absorption

Outside of strong absorption bands, the coupling between scattering and gaseous absorption is weak. This assumption leads to express the apparent reflectance as :

$$\rho^{*} \approx \rho_{na}^{*} T_g \tag{04}$$

where ρ_{na}^{*} is the signal ignoring the gaseous absorption and T_g the gaseous transmittance, which can be calculated from simulations. Ozone absorption and scattering processes are decoupled because the O_3 layer is located above the aerosols and mostly above the molecules. This remark can be altered if we have major stratospheric contamination.

For the water vapour, the scale height is roughly the same as the aerosol one. Nevertheless, even in the water band, the coupling term remains weak.

To account for the interactions between scattering and absorbing properties, we define:

$$T_g^c = \frac{\rho^{*}}{\rho_{na}^{*}}, \tag{05}$$

instead of simply computing the gaseous transmittance without the scattering effect.

b) Modeling Rayleigh scattering

A schematic model is to consider a two-layer model: molecules over aerosols. An illustration of this approximation is given in the worst case for nadir observations at 410 nm. The continental aerosol model was used with a visibility of 23 km. The results are plotted in Figure 2 as the relative difference between the reference multi-layer model and the two-layer approximation. Thus, the Rayleigh contribution above the aerosol-ground system can be written as:

$$\rho_{na}^{*} = \rho_R + T_R(\mu_s) \frac{\rho_{aG}}{1 - \rho_{aG} \cdot S_R} T_R(\mu_v) \tag{06}$$

where ρ_{na}^{*} is the top of atmosphere reflectance, ρ_R the Rayleigh reflectance, ρ_{aG} the aerosol-ground system reflectance, $T_R(\mu_s)$ and $T_R(\mu_v)$ the downward and upward Rayleigh transmittance respectively and S_R the spherical albedo relating to molecules. This expression correctly accounts for scattering processes above the aerosol-ground system with the suitable weight among all of the contributors. The only limitation lies in the assumption that the aerosol-ground system is quite lambertian (Table 2). The directionality of the signal below the molecule layer is mainly due to the aerosols. Because atmospheric contribution is high and combined to a generally lower surface reflectance, this modeling is more challenging at short wavelengths.

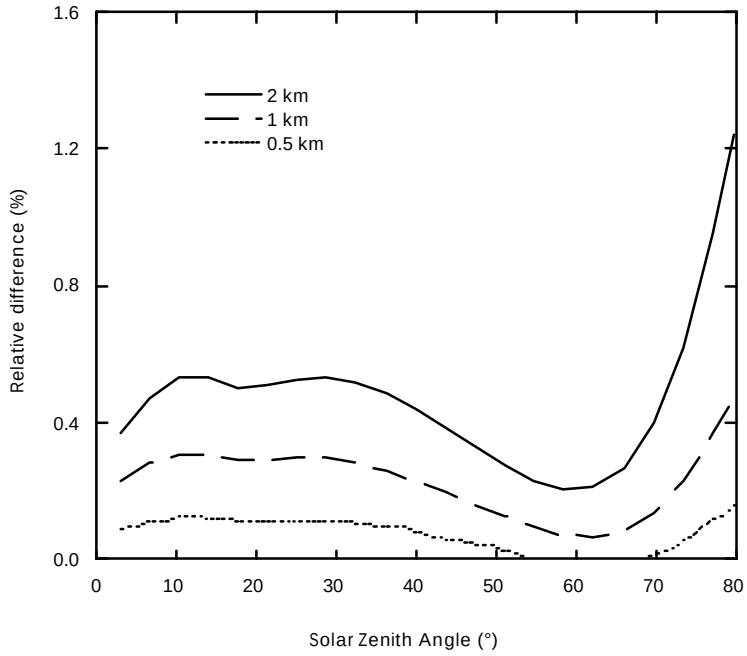

Figure 2: Relative influence of the aerosol scale height for H = 0.5, 1.0 and 2.0 km by reference to an aerosol layer below the molecules.

	V=23 km			V=08 km		
	(1)	(2)	(3)	(1)	(2)	(3)
λ=410 nm						
θ_s=0°	0.18721	0.08640	0.18579	0.20516	0.10996	0.20388
θ_s=30°	0.18153	0.07614	0.17677	0.19691	0.09455	0.19054
θ_s=60°	0.20138	0.08036	0.19296	0.22143	0.10756	0.21130
λ=440 nm						
θ_s=0°	0.17012	0.09654	0.16805	0.18687	0.11700	0.18471
θ_s=30°	0.16376	0.08658	0.15981	0.17734	0.10164	0.15981
θ_s=60°	0.18032	0.08927	0.17109	0.18032	0.08927	0.17109
λ=560 nm						
θ_s=0°	0.15538	0.13091	0.15510	0.16685	0.14331	0.16669
θ_s=30°	0.14789	0.12221	0.14715	0.15450	0.12869	0.15315
θ_s=60°	0.15301	0.12095	0.14912	0.16351	0.13100	0.15812

Table 2: For the continental model, we computed (1) the signal observed at nadir over vegetation in 3 MERIS bands, (2) the same computations but without Rayleigh scattering, and (3) the actual signal correctly retrieved when adding the molecular atmosphere above the ground+aerosol system and using the 5S approximations.

According to Equation (06), we can easily correct for Rayleigh to get the reflectance above the aerosol+ground system with:

$$\rho_{aG}^{c} = \left(\rho_{na}^{*} - \rho_{R}\right) \frac{1}{T_R\left(\mu_s\right) T_R\left(\mu_v\right)} \tag{07}$$

$$\rho_{aG} = \frac{\rho_{aG}^{c}}{1 + \rho_{aG}^{c} . S_R} \tag{08}$$

Because of the variation of the barometric pressure due to terrain elevation, all Rayleigh scattering functions will be pre-computed as a function of optical thickness instead of for each MERIS bands. In order to reduce the dimension of the LUTs related to the Rayleigh reflectance computations, we proposed several simplifications. The idea is (1) to use a Fourier series expansion to cancel the dependency in azimuth φ, (2) to treat the scattering phenomenon as primary scattering

corrected by a term due to multiple scattering, and (3) to compute this correction using polynomial regressions.

(1) First, we expand the Rayleigh reflectance for each MERIS band as a Fourier series:

$$\rho_R(\mu_V,\mu_S,\varphi)=\sum_{s=0}^{2}(2-\delta_{0,s})\rho_R^{(s)}(\mu_V,\mu_S)\cos s\varphi \qquad (09)$$

where $\delta_{0,s}$ is the Dirac's Function and where s is the order of the series.

(2) For each term of the Fourier series, $\rho_R^{(0)},\rho_R^{(1)},\rho_R^{(2)}$, we correct for the primary scattering $\rho_{R,P}^{(s)}$ also expanded in a Fourier series as for Equation (09). This primary scattering is expressed by an analytical formulation for the Rayleigh Phase Function for each Fourier series term:

$$P^{(0)}(\Theta)=\frac{3}{4}A\left[1+\cos^2(\theta_s)\cos^2(\theta_v)+\frac{\sin^2(\theta_s)\sin^2(\theta_v)}{2}\right]+B \qquad (10a)$$

$$P^{(1)}(\Theta)=-\frac{3}{4}A\cos(\theta_s)\cos(\theta_v)\sin(\theta_s)\sin(\theta_v) \qquad (10b)$$

$$P^{(2)}(\Theta)=\frac{3}{16}A\sin^2(\theta_s)\sin^2(\theta_v) \qquad (10c)$$

with A and B as defined in Equ. (01), and an analytical expression for the primary scattering:

$$\rho_{R,P}^{(s)}=\frac{P^{(s)}(\Theta)}{4(\mu_S+\mu_v)}\left(1-e^{-\delta_R\left(\frac{1}{\mu_s}+\frac{1}{\mu_v}\right)}\right) \qquad (11)$$

We introduce here a multiplicative factor to correct for multiple scattering:

$$f_R^{(s)}(\delta_R)=\frac{\rho_R^{(s)}}{\rho_{R,P}^{(s)}} \qquad (12)$$

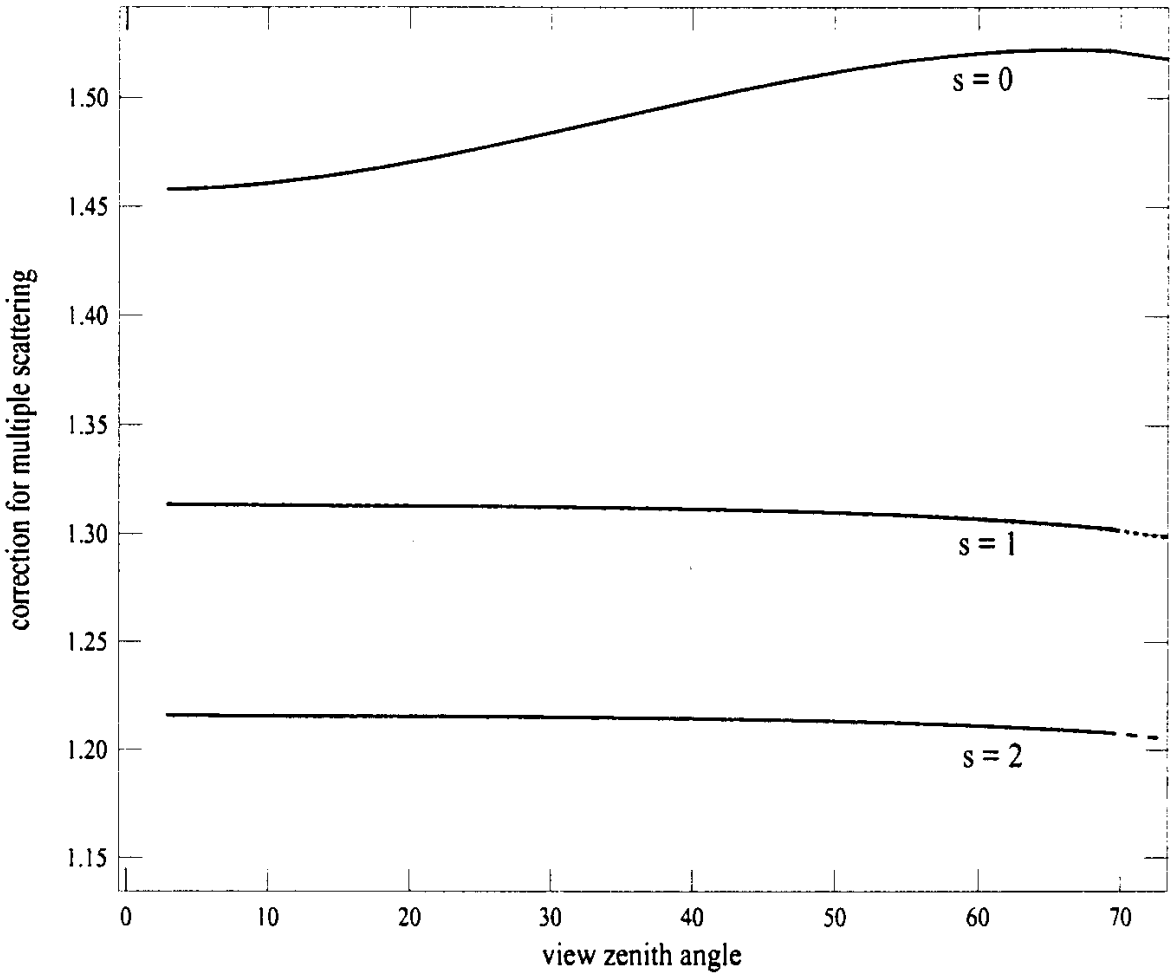

Figure 3 Correction functions for Rayleigh multiple scattering as a function of view zenith angle for θ_s = 73° and δ_R = 0.3; exact computations (dashed lines) are overlapped by a third order polynomial fit (solid lines).

With the SOS code, these 3 functions $f_R^{(s)}(\delta_R)$ have been computed and fitted by a third order polynomial in δ_R. Figure 3 illustrates the smooth behavior of these functions versus the viewing angle and the correct retrieval by a third order polynomial even for this extreme solar zenith angle. In the same way and for a given geometry (Figure 4) the dependence in optical thickness is easily modeled here by a second order polynomial fit.

The Rayleigh transmittance $T_R(\mu, \delta_R)$ has been computed using the SOS code and compared with the Vermote and Tanré analytical formula (Vermote and Tanré, 1992):

$$T_R^V(\mu,\ \delta_R) = \frac{(2/3 + \mu) + (2/3 - \mu)\, e^{-\delta_R/\mu}}{4/3 + \delta_R} \tag{13}$$

This formula has a relative accuracy of 0.1% for transmittance ranging from 1.0 to 0.6, but presents some discrepancies for lower transmittances. For MERIS, the environment allows extreme transmittances of 0.4. Therefore, a polynomial regression of the exact case versus this formula needs to be applied:

$$T_R(\mu,\ \delta_R) = \alpha_0 + \alpha_1\, T_R^V(\mu) + \alpha_2\, T_R^{V2}(\mu) \tag{14}$$

Figure 5 illustrates this technique.

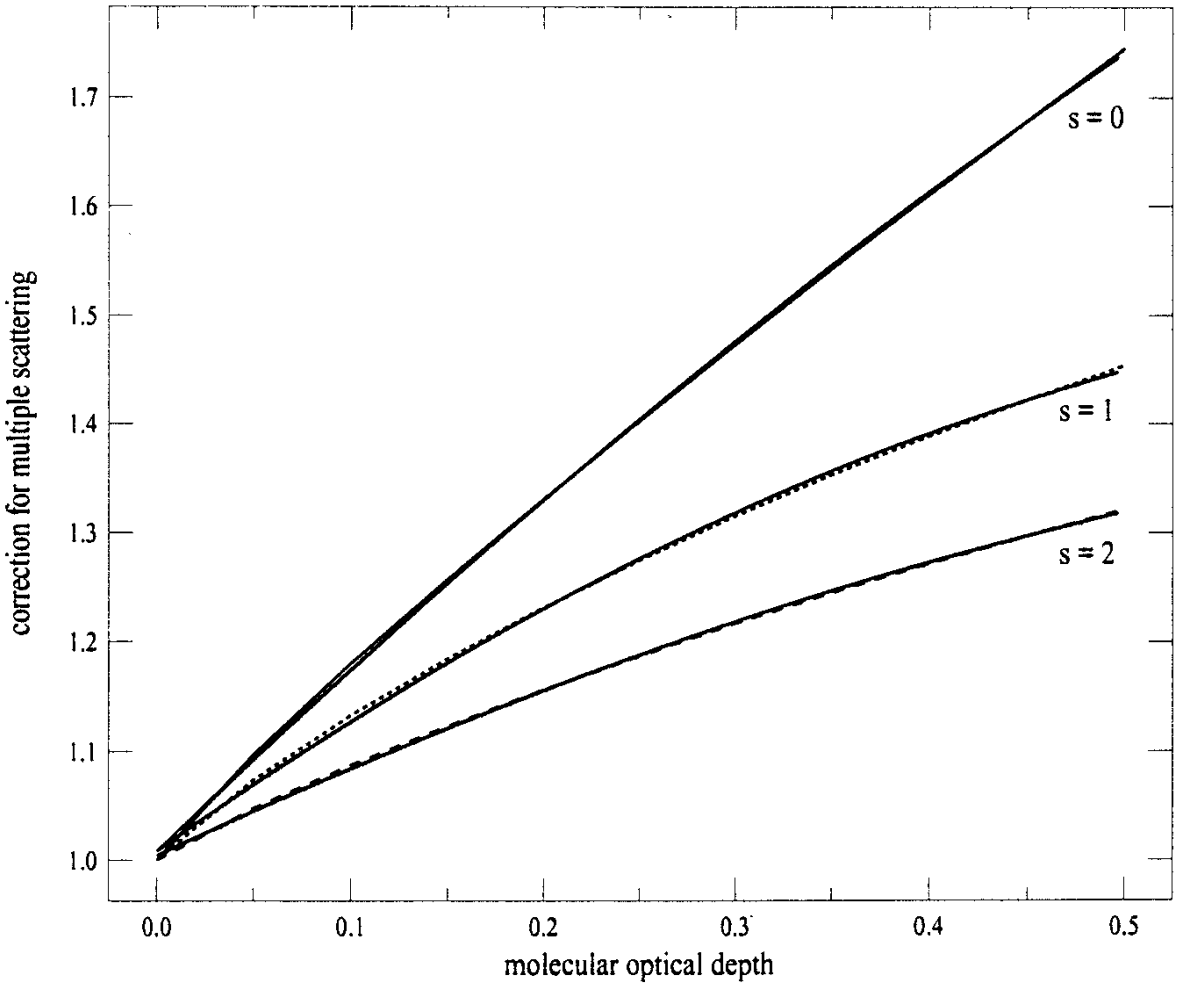

Figure 4: Correction functions for Rayleigh multiple scattering as a function of δR for $\theta_s = 62^o$ and $\theta_v = 32^o$; exact computations (dashed lines) are overlapped by a second order polynomial fit (solid lines).

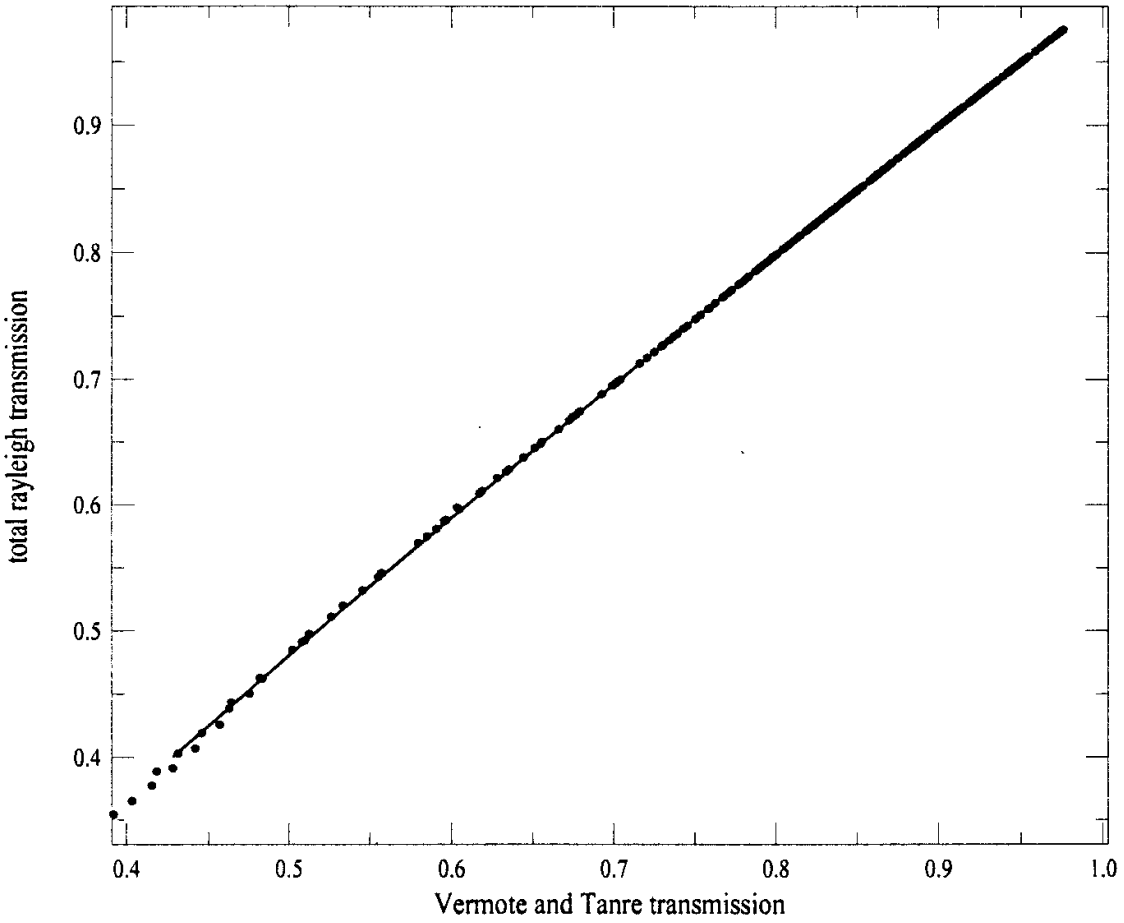

Figure 5: Representation of the total Rayleigh transmittance as a function of the Rayleigh transmittance as defined by Vermote and Tanré, 1992.

The spherical albedo $S_R(\delta_R)$ will be precomputed for 16 δ_R values ranging from 0.02 to 0.32.

c) Correcting for aerosol scattering

For the aerosol-ground contribution ρ_{aG} we use the same approach as for the Rayleigh :

$$\rho_{aG} = \rho_a + T_a(\mu_s)\frac{\rho_G}{1 - \rho_G \, . \, S_a} T_a(\mu_v) \qquad (15)$$

where ρ_a, T_a and S_a are respectively the intrinsic reflectance, the transmittance and the spherical albedo relative to the aerosols and ρ_G is the surface reflectance.

Using Equation (15), we can deduce the surface reflectance ρ_G from the top of aerosol reflectance:

$$\rho_a^c = (\rho_{aG} - \rho_a) \frac{1}{T_a(\mu_s)\, T_a(\mu_v)} \tag{16}$$

$$\rho_G = \frac{\rho_a^c}{1 + \rho_a^c \,.\, S_a} \tag{17}$$

Due to poor knowledge of aerosols, we will consider the simplest but realistic description for the size distribution by a power law :

$$n(r) \approx r^{\alpha - 3} \tag{18}$$

where the Angström coefficient α describes the wavelength dependency (λ) of the aerosol optical thickness δ_a:

$$\frac{\delta_a(\lambda)}{\delta_a(\lambda')} = \left(\frac{\lambda}{\lambda'}\right)^{\alpha} \tag{19}$$

For MERIS, we will use 12 aerosol models defined by 4 values of α (0.0, -0.5, -1.0, and -1.5) and 3 values for the real part of the refractive index *m* (1.33, 1.44 and 1.55). These models are close to those proposed for the POLDER ground segment which will probably be used for our aerosol climatology data base. With a Junge power law, the phase matrix does not depend on wavelength, and the main parameter is the phase function. So for the 12 aerosol models, we generated these phase functions into LUTs for 83 scattering angles. Thus, for a given aerosol model, we just need to model the dependence in δ_a (we will see in the next section how to determine the model).

The computation of the aerosol reflectance is based on the same idea as for the Rayleigh reflectance e.g. decoupling primary and multiple scattering and use of the Fourier series expansion. But here, we first correct for the primary scattering $\rho_{a,P}$ and only the residual function is expanded into a Fourier series:

$$f_a(\varphi,\delta_a) = \frac{\rho_a(\varphi,\delta_a)}{\rho_{a,P}(\varphi,\delta_a)} = \sum_{s=0}^{n} a_a^{(s)}(\delta_a)\cos(s\varphi) \qquad (20)$$

The Fourier series has been applied to the function f_a in place of the aerosol reflectance ρ_a because f_a is less sensitive to the azimuth φ than ρ_a. Therefore, the order of the series can be reduced. For aerosols, the number of orders of the Fourier series expansion applied to ρ_a can reach 80 (in place of 3 for the Rayleigh). A study for continental aerosols has shown that it was possible to reduce the order of the Fourier series applied to f_a to 6 terms (then n = 5 in Equation (20)) as illustrated in Figure 6. Consequently, we just fitted 6 functions $a_a^{(s)}(\delta_a)$ by a polynomial regression versus aerosol optical thickness. As for Rayleigh multiple scattering correction, a third order polynomial is suitable for aerosol optical thicknesses δ_a ranging from 0.05 to 1.5. To compute the primary scattering term, we just need the phase function and the single scattering albedo.

The aerosol phase function is precomputed at 83 angles and multiplied by the single scattering albedo. A very similar analytical expression to Equation (11) is used to compute the primary scattering.

The total transmission T_a, for the direct to direct path, is equal to $T_a(\mu_s).T_a(\mu_v)$. For each aerosol model, for 12 zenith angles, and for 15 values of δ_a, we have LUTs to extract $T_a(\mu)$. The spherical albedo for a given aerosol model is computed versus 15 values of δ_a.

3.2. Numerical Description

3.2.1. The gaseous correction module

The gaseous transmittance is the product of the two following transmittances:

(1) ECMWF (or other source) provided the total ozone content in the atmospheric column, U_{O_3}. The total air mass m is equal to $1/\mu_s + 1/\mu_v$. The ozone transmittance is defined as:

$$T_{O_3} = e^{\left(-U_{O_3}\, m\, \delta_{O_3}\right)} \qquad (21)$$

with δ_{O_3} as given in Table 1.

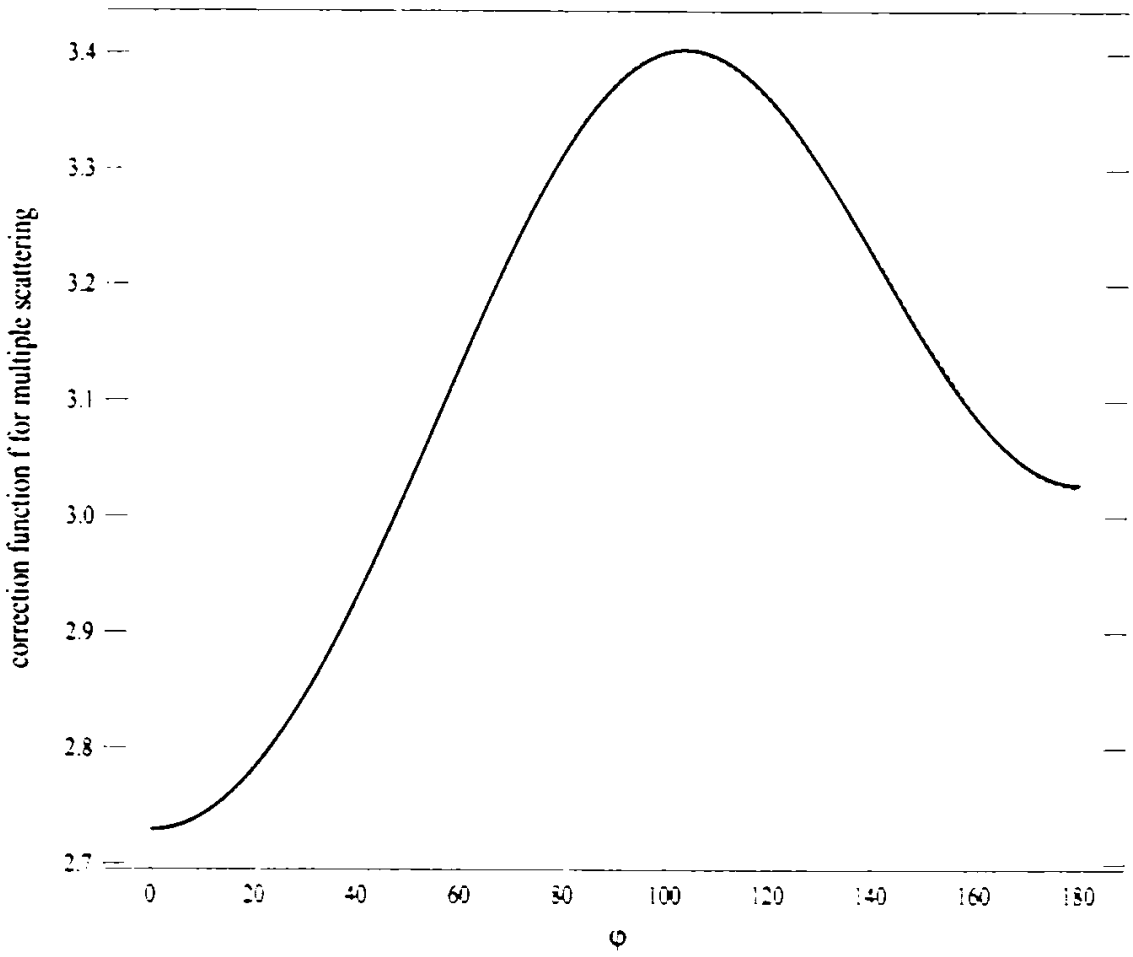

Figure 6: Azimuthal dependency of f for m = 1.44, ν = -4.5, $\theta_s = 73^o$, $\theta_v = 32^o$ and $\delta_a = 0.6$; exact computations (dashed lines) are overlapped by a second order polynomial fit (solid lines).

(2) To estimate the water vapour transmittance, one possibility is to compute the transmittance from the water vapour content as derived from the ratio 900 nm / 890 nm. However, some uncertainties appear because of the coupling between scattering and absorption, mainly above dark targets and for low atmospheric visibilities. Figure 7 shows that the water vapour transmittance is not well correlated with the two band ratio 900 nm / 890 nm because of multiple scattering effects. Calculations have been performed for various aerosol visibilities (from 50 to 8 km), surface reflectances (vegetation, sand and bare soil (0.2)) and geometrical conditions (solar angles of 30 and 60^o and viewing angles of 0 and 40^o). This curve has to be compared with Figure 8 where water vapour transmittance is calculated accounting for multiple scattering effects and which is well correlated with the two band ratio. The surface reflectance is assumed to be the same in the two

adjacent bands. The aerosol scattering does not vary significantly as well. Of course, because we now include the coupling in our definition of the transmittance, we have a straight line. This line departs from the first bisector because the residual gaseous transmittance at 890 nm is included in the two band ratio (see Table 1).

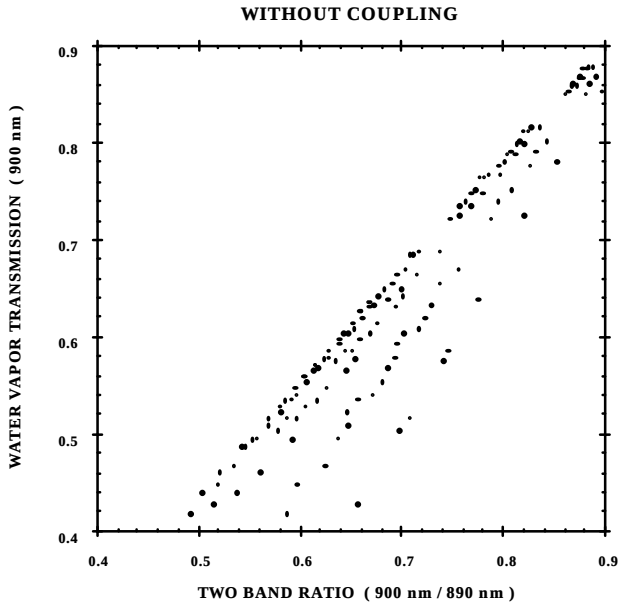

Figure 7: Gaseous transmittance in the 900 nm MERIS band as a function of the ratio 900 nm / 890 nm, calculated without multiple scattering effects and with an aerosol content ranging from 50 to 8 km, for various surface reflectances and geometrical conditions.

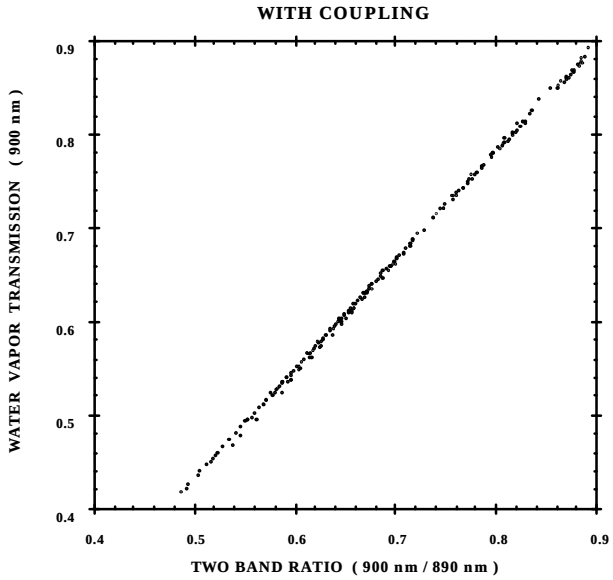

Figure 8: Same as Figure 7 but accounting for multiple scattering effects.

Our primary goal is not to obtain U_{H_2O} but only to be able to correct MERIS channels for the H_2O absorption, including the coupling term. Because coupling acts in the different bands, we can reduce its influence in a direct relationship between the ratio 900 nm / 890 nm and T_g^c at 705 nm.

As shown in Figure 9, a good fit by a second order polynomial allows a good retrieval of the transmittance at 705 nm if we measure the ratio 900 nm / 890 nm. This fit is quite accurate regardless of aerosol content and surface reflectance. Here we ran cases for aerosol visibilities ranging from 8 to 50 km, solar angles of 30, 60^o and 75^o, viewing angles of 0 and 40^o, tropical, mid-latitude summer and winter atmospheres, and various surface types (same conditions as above).

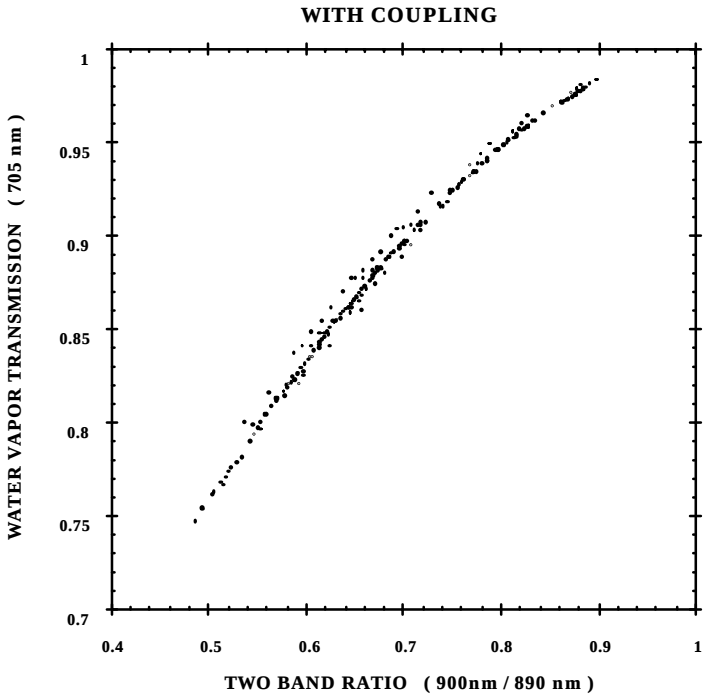

Figure 9: Corrected water vapour transmittance in the 705 nm MERIS band as a function of the ratio 900/890 nm.

To simply quantify the gain in accuracy of a direct association between the two band ratio and the water vapour transmittance at 705 nm, let us suppose that we have a water vapour content corresponding to a water vapour transmittance of 0.6 at 900 nm. Depending on the surface reflectance and on the aerosol loading, the two band ratio ranges between 0.64 and 0.76 (see Figure 7). This range gives, according to Figure 8, a water vapour transmittance between 0.86 and 0.93. In comparison, a direct association between the two band ratio and the 705 nm transmittance reduces the error domain to approximately 0.02 (Figure 8).

The same technique is applied to each MERIS channel where absorption by water vapour continuum is non negligible, meaning all bands except 490, 442.5 and 412.5 nm. We also foresee applying this principle to estimate the O_2 transmittance at 775.5 nm from the 760 nm / 753.75 nm ratio if necessary.

Satellite reflectances ρ^* are corrected from gaseous absorption T_g assuming Equation (05):

$$\rho^*_{ng} = \frac{\rho^*}{T_g^c} \tag{22}$$

with ρ^* and ρ^*_{ng} measured and corrected reflectances respectively.

This correction for water vapour is performed on a pixel-by-pixel basis.

3.2.2. The Rayleigh correction module

3.2.2.1. Surface pressure determination from O_2 channel

The Rayleigh optical thicknesses are determined for a surface pressure of 1013 hPa, but in the algorithm we have to take into account the real surface pressure to be accurate. One possibility is to use ECMWF data combined to digital maps. Because of the low spatial resolution of the digital maps (the elevation is provided every 64x64 full resolution pixels i.e. approximately every 18 km), we prefer here to derive the pressure from the MERIS data themselves.

Several techniques have been used in the past to estimate the cloud top pressure (Fischer and Grassl, 1991) or the surface pressure (Mitchell and O'Brien, 1987; Bréon and Bouffiès, 1996) from measurements in the "A" oxygen absorption band. At this wavelength, the radiation reflected by the surface and measured at the top of the atmosphere is mainly depending on oxygen absorption and therefore on the surface elevation.

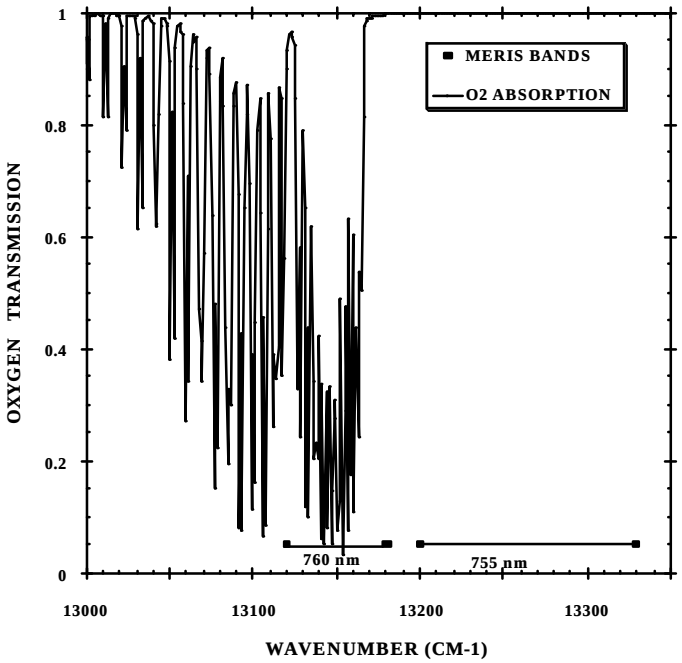

Figure 10 : Oxygen transmittance in the two MERIS channels used for the determination of surface pressure. The oxygen transmittances were calculated with a line-by-line model.

MERIS carries two channels allowing an estimate of the surface pressure P_S (Figure 10). Assuming no scattering effects in a first approximation, we have calculated with a line-by-line model the ratio *R* of the reflectance measured in the MERIS oxygen band (760 nm) and in the non-absorbing contiguous channel (753.75 nm) for a large number of geometries (air mass *m* ranging from 2 to 6) and surface pressures (ranging from 1050 to 600 hPa). Since we can neglect the small spectral variation of the ground between the two adjacent bands, *R* represents here the gaseous transmittance at 760 nm. Figure 11 shows the ratio *R* as a function of the product $m\ P_S^2$: the surface pressure is well correlated to the reflectance ratio *R*. This curve can be fitted with a sixth order polynomial and knowing the air mass *m* we have a simple determination of P_S.

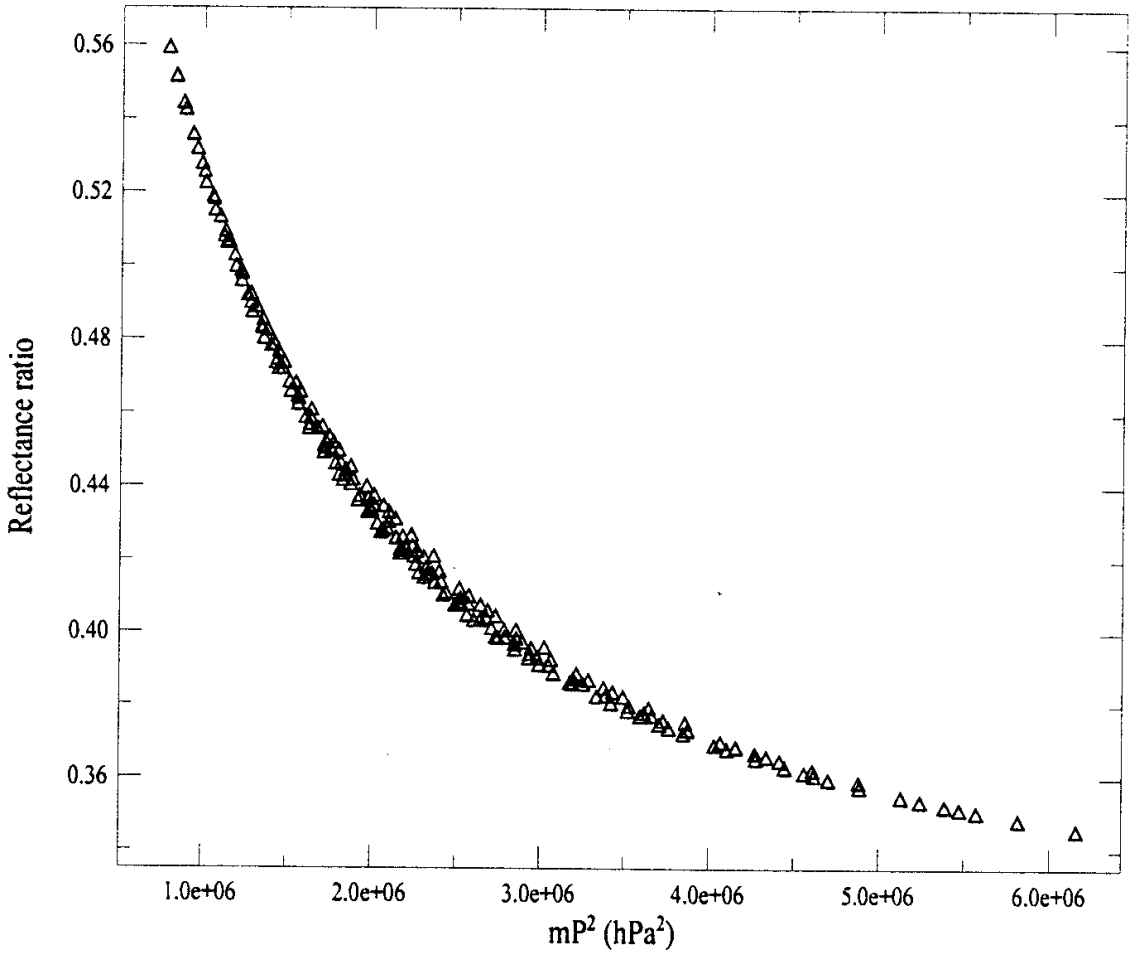

Figure 11: Reflectance ratios, calculated from a line-by-line model, as a function of the product of the air mass m and the square of surface pressure P_S, for a large number of geometries (m ranging from 2 to 6).

However in practice the apparent pressure determined from MERIS measurements can be affected by interactions between absorption and scattering effects. We performed calculations to evaluate the impact of aerosols and molecular scattering on the surface pressure retrieval. The ratio R is mainly depending on the surface reflectance ρ_G, solar and viewing geometrical conditions (θ_s, θ_v), the aerosol optical thickness δ_a and the surface pressure P_s:

$$P_s = f\left(\rho_G,\ \delta_a,\ \theta_s,\ \theta_v\right). \tag{23}$$

For instance, Figure 12 shows the variation of the reflectance ratio accounting for multiple scattering effects.

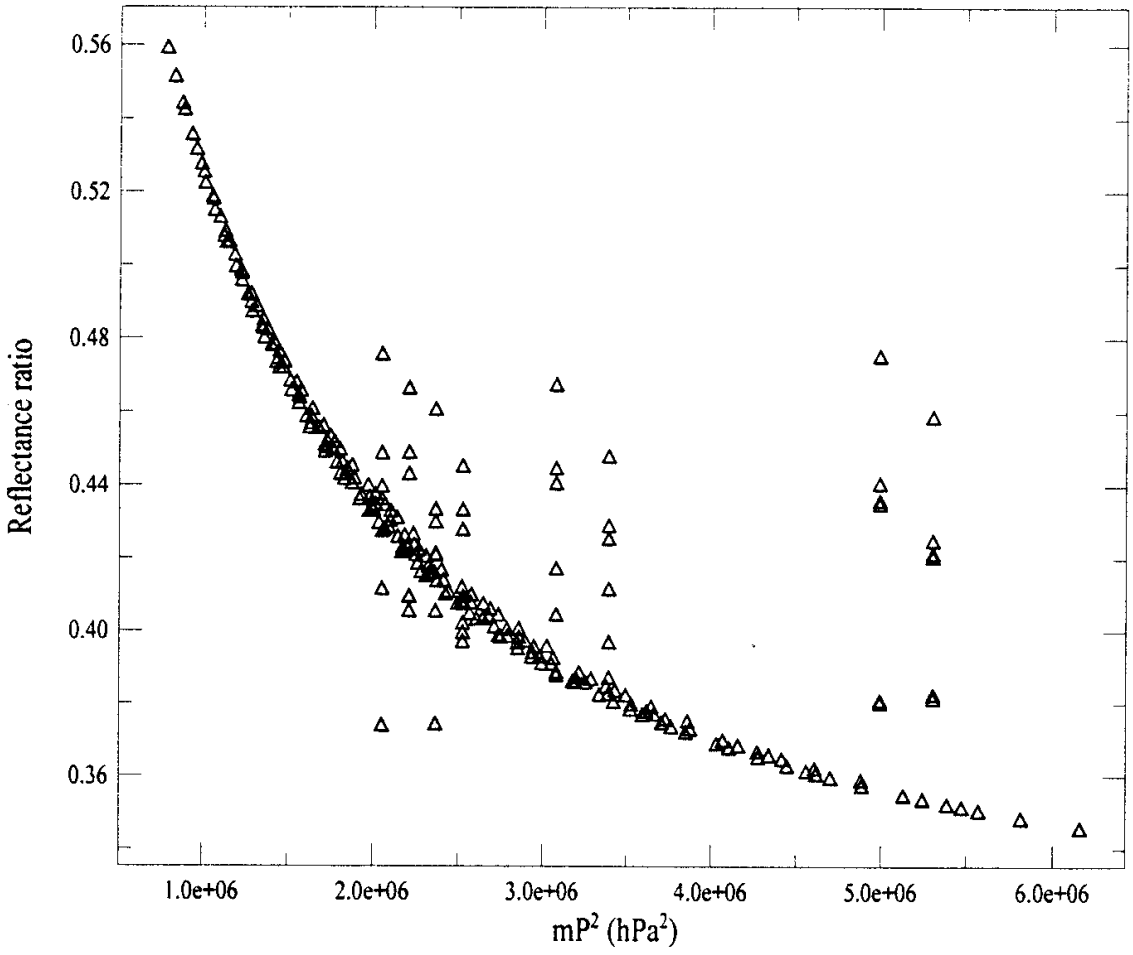

Figure 12: Variations of the reflectance ratio (760 nm / 753.75 nm) calculated with a line-by-line model and the discrete ordinate method as a function of the product of the air mass m and the square of the surface pressure in the following conditions: θ_S = 30, 60 and 75°, ρ_G = 0.05, 0.25 and 0.45, θ_V = 0 and 40°, δ_a = 0.1 and 0.5 and with molecular scattering.

The ratio *R* can be calculated for realistic atmospheric conditions from the GAME radiative transfer model as a function of ρ_G, θ_S, θ_V, δ_a and P_S, to set up a look-up table. From atmospheric parameters and LUTs, the surface pressure P_S can be fitted according to the ratio measured by MERIS.

However, for practical studies, atmospheric parameters are not accurately known. Thus, if geometrical conditions are well defined, the variation in surface pressure ΔP_S can be evaluated as a function of uncertainties on atmospheric parameters $\Delta\rho_G$ and $\Delta\delta_a$ as:

$$\Delta P_S = \sqrt{\left(\frac{\bullet P}{\bullet \rho_G}\Delta\rho_G\right)^2 + \left(\frac{\bullet P}{\bullet \delta_a}\Delta\delta_a\right)^2}\ , \tag{24}$$

or

$$\Delta P_S = \sqrt{\left(\Delta P_{\rho_G}\right)^2 + \left(\Delta P_{\delta_a}\right)^2}\ . \tag{25}$$

The partial derivatives in Equation (24) can be calculated from the LUT to estimate the variation of surface pressure ΔP_S.

To evaluate uncertainties defined in Equation (25), radiances have been calculated for the two MERIS channels presented in Figure 11 using the following conditions: surface reflectance equal to 0.2, 0.3 and 0.4, an aerosol optical thickness of 0.1, 0.3 and 0.6, a surface pressure of 1013, 899, 795 and 701 hPa, a solar zenith angle of 30, 60 and 75°, and a view zenith angle of 0°.

We have reported in Table 3 variations ΔP_S of surface pressure calculated using GAME and Equation (25), with the following conditions :

$$\rho_G = 0.3 \pm 0.05 \qquad \delta_a = 0.3 \pm 0.1 \quad \theta_V = 0^o$$

P_s (hPa)		30°	60°	75°
1013	$\Delta P\rho_G$	6.0	7.4	14.1
	$\Delta P\delta_a$	1.9	2.1	21.5
	ΔP_s	6.3	7.7	25.7
899	$\Delta P\rho_G$	4.5	5.4	10.3
	$\Delta P\delta_a$	1.8	0.6	12.8
	ΔP_s	4.8	5.4	16.4
795	$\Delta P\rho_G$	3.2	3.7	6.8
	$\Delta P\delta_a$	1.5	0.3	6.9
	ΔP_s	3.5	3.7	9.7
701	$\Delta P\rho_G$	2.4	2.8	4.9
	$\Delta P\delta_a$	1.2	0.5	4.0
	ΔP_s	2.7	2.8	6.3

Table 3: Uncertainties on the surface pressure ΔP_S (in hPa) as a function of solar zenith angle θ_s (ΔP_{ρ_G} and $\Delta P_{\delta a}$ represent the uncertainties on P_S due to $\Delta\rho_G$ and $\Delta\delta_a$ respectively). These simulations have been performed for the following conditions:

$\rho_G = 0.3 \pm 0.05$ $\delta_a = 0.3 \pm 0.1$ $\theta_v = 0^o$

The variation of the surface pressure ΔP_S is less than 10 hPa for solar zenith angles lower than 60°, but can reach 25 hPa for low solar elevation (• 75°). These differences show that the interactions between absorption and scattering effects become non-negligible for low solar elevations.

However, this technique has two major inconveniences in the atmospheric correction framework: (1) it requires building a large look-up-table covering a realistic variety of atmospheric or geometrical conditions and a large number of interpolations; (2) it requires knowledge of surface reflectance and aerosol optical thickness, implying considerable complications to the atmospheric correction algorithm since these parameters are not known at this stage of the algorithm.

We have then calculated with GAME the ratio between the transmittance in the oxygen band without scattering effect and that accounting for scattering effects. Transmittance ratio probability are reported in Figure 13 as a function of the surface reflectance and for aerosol visibilities ranging from 8 to 50 km. Interactions between scattering and absorption are negligible for a transmittance ratio equal to 1. Standard deviations (ΔR^a) and mean transmittance ratios are reported on these curves and show the influence of the surface:

- For bright surfaces, mean transmittance ratio is almost equal to 1 and standard deviation is weak. Neglecting aerosol scattering effects has no dramatic consequences on surface pressure retrieval (error less than 1% on the transmittance ratio).

- For dark surfaces, radiation scattering is no longer negligible but standard deviation remains weak, on the order of a few percent.

The idea is then to retrieve the surface pressure from reflectance ratio calculated without scattering effects (from Figure 12). To take surface effects into account, this reflectance ratio can be modified using a correction factor depending on surface reflectance and the airmass. Since surface reflectance is not known, this correction factor can be determined from apparent reflectances at the top of the atmosphere at 753.75 nm where surface reflectance is the main contributing factor.

Errors ΔR^b originating from using apparent reflectances instead of surface reflectances have been evaluated from simulations with an aerosol visibility of 23 km. Errors ΔR^b presented in Table 4 have been calculated using a visibility of 8 km with continental aerosols. The total error on transmittance ratio ΔR^T is then defined as:

$$\Delta R^T = \sqrt{\left(\Delta R^a\right)^2 + \left(\Delta R^b\right)^2} . \qquad (26)$$

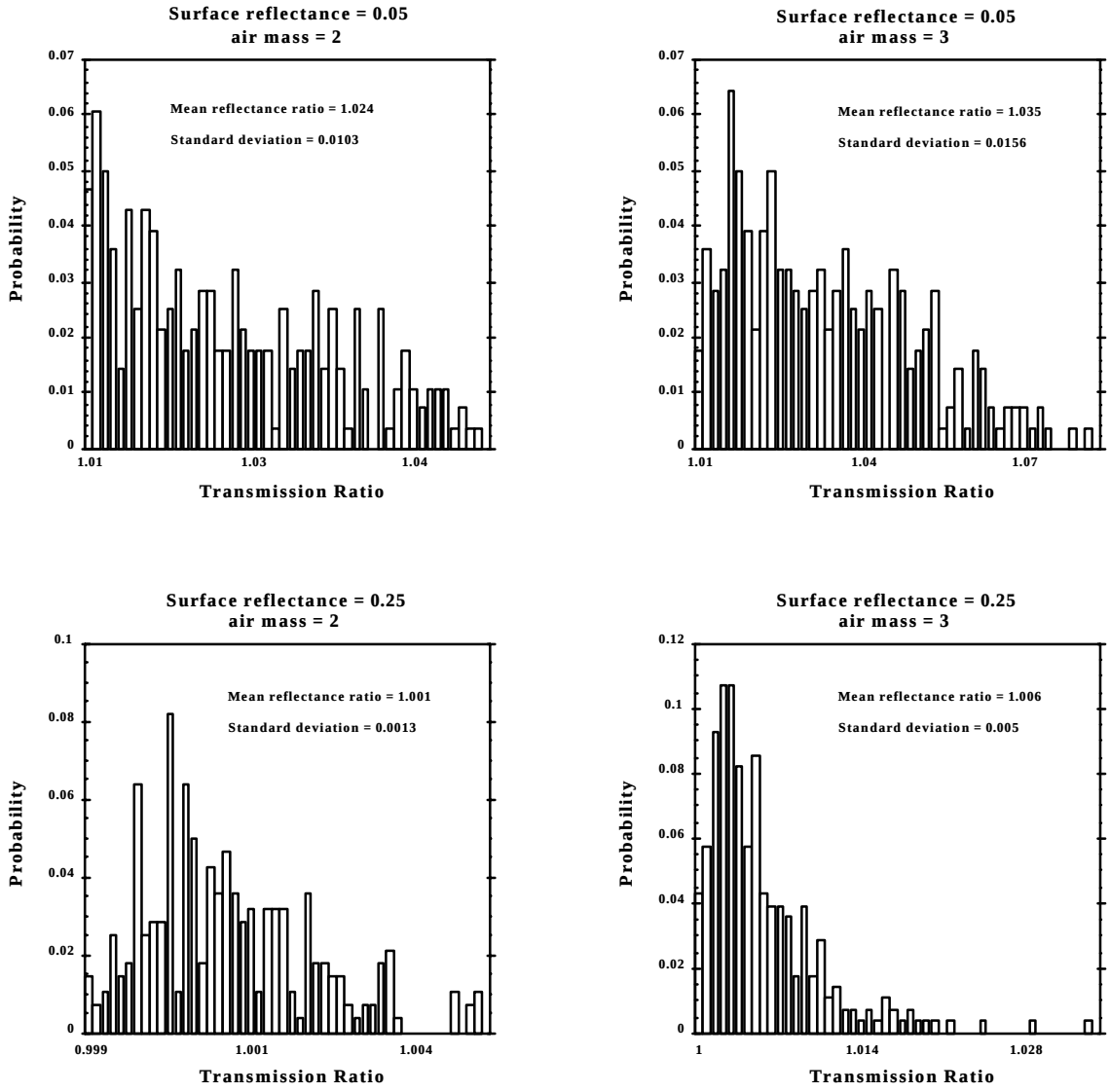

<u>Figure 13:</u> Transmittance ratio probability as a function of surface reflectance and air mass, for aerosol visibilities ranging from 8 to 50 km. Standard deviations and mean transmittance ratios are presented on the curves.

The maximum error is on the order of 1 % on the transmittance ratio for a dark surface and of a few tenth of a percent for a bright surface, therefore on the same order of magnitude as the accuracy expected on the calibrated MERIS radiance data. As an example, deviations from the surface pressure have been reported in Table 4 for total air masses of 2 and 3 and accounting for

total error ΔC on the corrective factor. In most cases, maximum errors on the surface pressure are less than 25 hPa and can reach 40 hPa for dark surfaces. This simple determination of the surface pressure does not present the same accuracy as the first approach we described above but offers the simplest operational scheme we can foresee.

ρ_S	0.05	0.05	0.25	0.25
airmass	2	3	2	3
C	1.024	1.035	1.001	1.006
ΔC^a	0.010	0.016	0.001	0.005
ΔC^b	0.005	0.01	0.001	0.002
ΔC^{Total}	0.011	0.019	0.001	0.005
P_S (hPa)	990	920	1050	1000
ΔP_S (hPa)	25	40	5	15

Table 4: Uncertainties on the surface pressure retrieval using reflectance ratio without scattering effects and correction factors as a function of surface reflectance.

The first estimate on the error on the pressure, the dispersion of the corrective factor C as well as the error induced by the use of the apparent reflectance instead of the surface reflectance, was done combining all geometries. If we introduce the dependence of C on the geometry, we can then expect to gain a factor of two on the accuracy of the pressure determination.

3.2.2.2. Rayleigh correction

The pressure is averaged on a 4*4 pixel window and the corresponding value is used to weight in proportion the optical thickness reported in Table 1. The Rayleigh atmospheric functions are computed for the mean geometrical conditions over the window. The Rayleigh correction follows Equations (07) and (08).

3.2.3. The aerosol remote sensing

To compute the aerosol functions, we assumed the knowledge of the aerosol properties, but the question is: how to get these properties? In fact, we thought about two possibilities which are usually adopted by the community. The first one consists in retrieving the aerosol optical properties from the data themselves, and the second one, when the former is not possible, is the use of an

existing aerosol climatology. For the time being, the climatology is not precisely defined but we think about using the POLDER product. In any case, the climatology will be used as a default option.

The aerosol remote sensing will be performed over dark dense vegetation (DDV, Kaufman and Sendra, 1988) for which a definition as well as the identification is reported in the ATBD on Pixel Identification (ATBD 2.17). Once we identified the DDV surfaces, we can retrieve aerosol properties assuming a standard value for the DDV reflectance in MERIS bands 1, 2 and 7 where the spectral reflectance is the lowest. Because different types of DDV are possible, we introduced the following models:

- three equatorial models between -20 and +20 degrees in latitude,
summer and winter, Africa, Asia and America.
- two tropical models between +/-20 and +/- 40, summer and winter, America and Asia.
- 4 mid-latitude models, summer and winter, West America, East America, Asia and Europe.
- two boreal models for summer, America and Eurasia.

These models were defined by the CESBIO.
The DDV method for aerosol remote sensing has been proposed and accepted for several projects on atmospheric correction over land, such as MODIS or VEGETATION and has been successfully used with data from the AVHRR instrument (Vermote et al., 1994) and the MODIS Airborne Simulator (MAS) (Roger et al., 1994).

For MERIS, the process starts with the selection of a refractive index for the aerosols from the climatology. We have then 4 aerosol models corresponding to 4 Angström coefficients. For each of them, we can compute the top of aerosol reflectance according to a 6S-like formulation of the signal similar to equation (15):

$$\rho_{aG} = \rho_a + \frac{T_a(\theta_s)\, T_a(\theta_v)\, \rho_{DDV}}{1 - s_a \rho_{DDV}} \qquad (27)$$

The DDV reflectance ρ_{DDV} is known for MERIS bands 1, 2, and 7. The atmospheric functions ρ_a, T_a, s_a , for a given aerosol model, depend solely on δ_a. We then loop on δ_a to retrieve the MERIS reflectances after gas and Rayleigh correction. This retrieval is performed for the 4 aerosol models in the 3 MERIS bands. We select the model for which the Angström coefficient is the closest to the one obtained from the δ_a retrieval. To take account for the BRDF effects over DDV for the aerosol retrieval,
An alternative method was developed (see ATBD 2.19).

We checked the opportunity for using one constant standard value per wavelength for the DDV reflectances. Using the BOREAS and POLDER data sets, we defined the surface reflectance for MERIS bands 2 and 7 as a mean value (respectively 0.016 and 0.030) and an uncertainty value (respectively 0.004 and 0.010). Using the 6S code, we tested the impact of these uncertainties on the aerosol optical thickness retrieval. Results (Figure 14) show that the impact is negligible in band 2 but appears more critical in band 7. So it clearly appears that we have to define a simple DDV reflectance model describing the dependency upon the solar and the viewing angle.

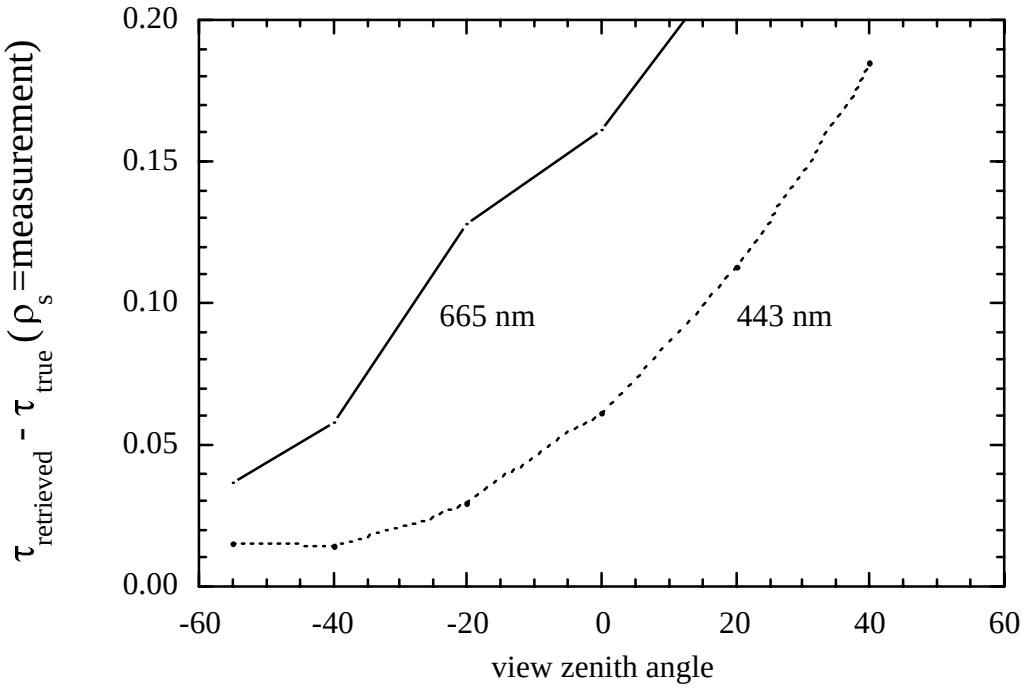

Figure 14: Example of error analysis for the aerosol optical thickness retrieval assuming a constant value for the surface reflectance of the DDV (0.016 at 443 nm and 0.030 at 665 nm). We assumed an error on the surface reflectance of 0.004 and 0.010 at 443 nm and 665 nm respectively. Computations have been performed with 6S and using the POLDER and BOREAS data sets.

Because of the impossibility to define an atmospheric correction on a pixel by pixel basis, we will open a window for which the atmospheric parameters will be determined as to be a constant or to be an averaged value over the window. The size of the window first depends on the spatial variability of the atmospheric parameters. For the gaseous contents, ozone and water vapour, they are provided by ECMWF on a grid of 50 km x 50 km. For the aerosols, we can refer to the aerosol product for

POLDER (30 km x 30 km) or for MODIS (50 km x 50 km). For the global coverage, 32 pixels along the scan lines correspond to a variation of 3^o for the view zenith angle. A theoretical study with 6S has shown that, along track, the variation of the solar zenith angle is less than 0.4^o inside a grid of 32 x 64 pixels, anywhere in the world. According to the above considerations, we will propose to use an area corresponding to 32 pixels along scan and to 64 pixels along track.

If we have a pure land window, we first assume that we need a certain number of DDV pixels to be representative (N_{test} = 32). If we have a mixed window with water and land, we first assume that the ocean branch provided the aerosol reflectances in MERIS bands 1, 2 and 7. If N_w is the number of ocean pixels suitable for atmospheric correction, N_L the corresponding number for land, then we can weight the aerosol reflectances as follows:

$$\rho_a = \alpha_w N_w \rho_a^w + \alpha_L N_L \rho_a^L / \alpha_w N_w + \alpha_L N_L \quad (28)$$

At start: $\alpha_w = \alpha_L = 1$. A more sophisticated weighting between land and water should results from an error analysis.

3.2.4. The aerosol correction module

The aerosol atmospheric functions are computed for the mean geometrical conditions for the window. The aerosol correction follows equations (16) and (17). The interpolation of aerosol fields applicable to all land pixels, from the Level 2 product, and the correction of surface reflectance for aerosols, are deferred to Level 3 processing.

3.3. The flow charts

Figure 15 proposes the flow chart for the atmospheric correction. This flow chart is applied to a 32*64 MERIS pixel window. The geometrical conditions are known for a 16*16 pixel grid (see MERIS Product Specification). It is not necessary to know geometrical conditions on a pixel-by-pixel basis because they don't vary much from one pixel to the next. We interpolate the solar zenith angle, the view zenith angle at the center of sub-windows of 4*4 pixels. The scattering angle is computed at the center of each sub-window. For the full resolution, all these dimensions need to be multiplied by 4.

The four main modules: gaseous correction (2.6.12), Rayleigh correction (2.6.15), aerosol model (2.6.17) and aerosol correction (2.6.18) are described above. The cloud heterogeneity flag

(2.1.3) is described in the ATBD on Pixel Identification (ATBD 2.17) and we will introduce the barometric pressure module (2.1.12) below. The numbers between parentheses refer to the architecture breakdown in the MERIS System Architecture Theoretical Basis Document.

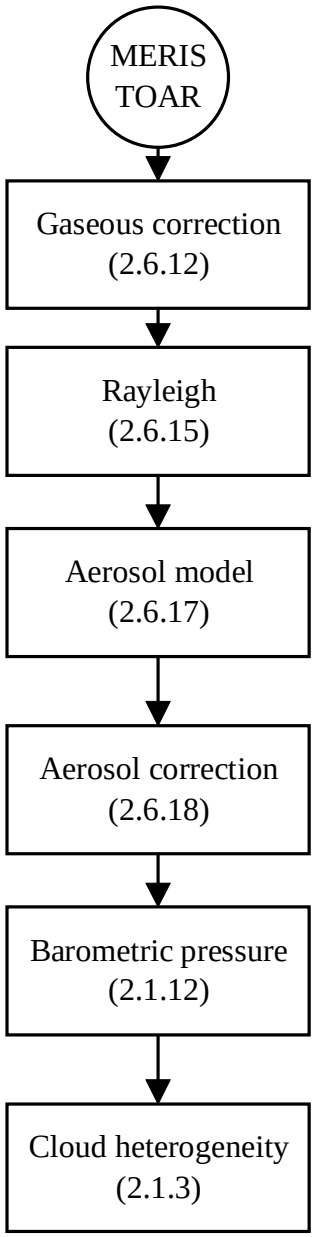

Figure 15: General flow chart for Atmospheric Correction over land (2.6).

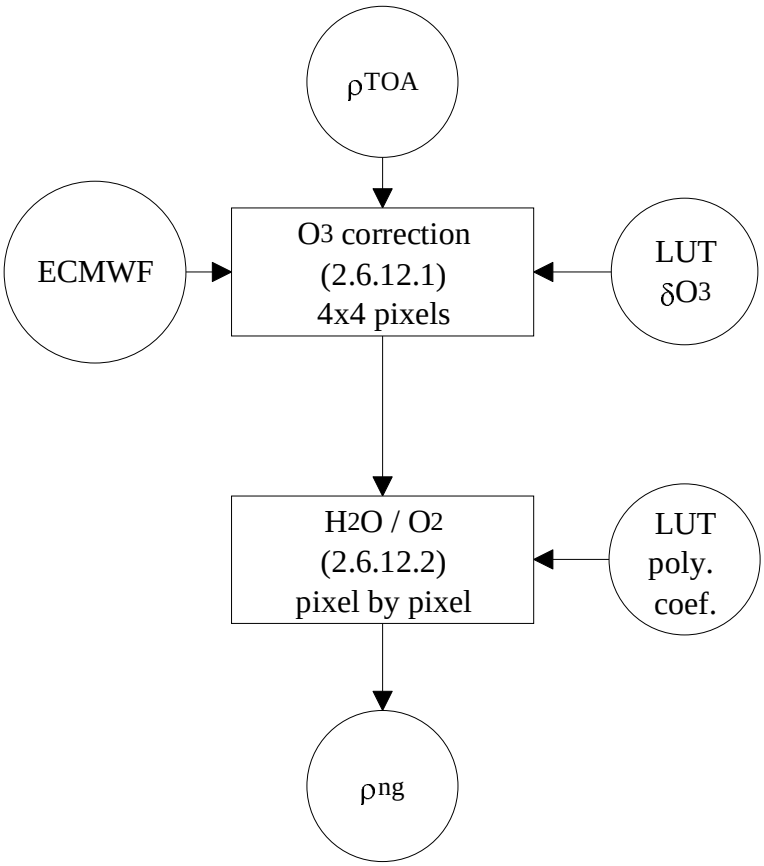

Figure 16: Gaseous correction flow chart.

Figure 16 shows the gaseous correction flow chart. ECMWF (or a similar source) is supposed to provide the ozone content. If not available, we will use climatologic values. In the O_3 correction module (2.6.12.1), the transmittance follows an exponential law according to Equation (21). Because of the small spatial heterogeneity of O_3, the correction is applied to a 4*4 pixel window. The ratio 900 nm / 890 nm gives the H_2O transmittance in all the MERIS bands affected by water vapour absorption (2.6.12.2). In this case, we can face large spatial variabilities of the water vapour content and the correction is performed on a pixel by pixel basis. With a small shift of MERIS band 13, we can avoid the O_2 absorption, therefore no correction is needed. The final outputs (2.6.1.3) are MERIS TOA reflectances for a non (gas) absorbing atmosphere.

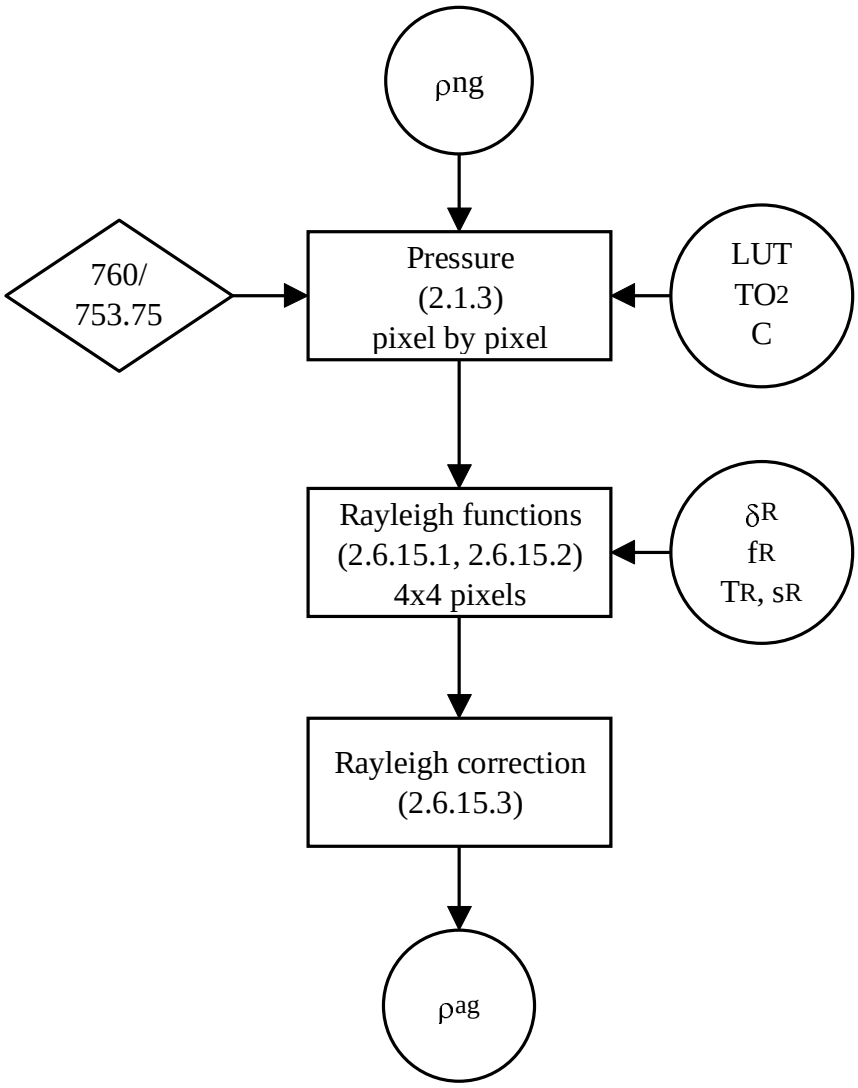

Figure 17: Rayleigh correction flow chart.

We start the Rayleigh flow chart (Figure 17) by a determination of the barometric pressure (2.1.3) based on the 760 nm / 753.75 nm ratio. Surface effects are taken into account by applying a correcting factor depending on apparent reflectance at 753.75 nm . The O_2 transmittance gives the barometric pressure averaged over the 4x4 pixel window.

Using the same geometry on a 4*4 pixel window with the mean pressure to compute δ_R., we extract the Rayleigh scattering functions from the LUTs (2.6.15.1, 2.6.15.2). Then we easily correct from the Rayleigh (2.6.15.3). The outputs are the MERIS top of aerosol reflectances.

The flow chart (Figure 18) for the determination of the aerosol model is more complex. The DDV pixels are flagged (see ATBD 2.17 on Pixel Identification).

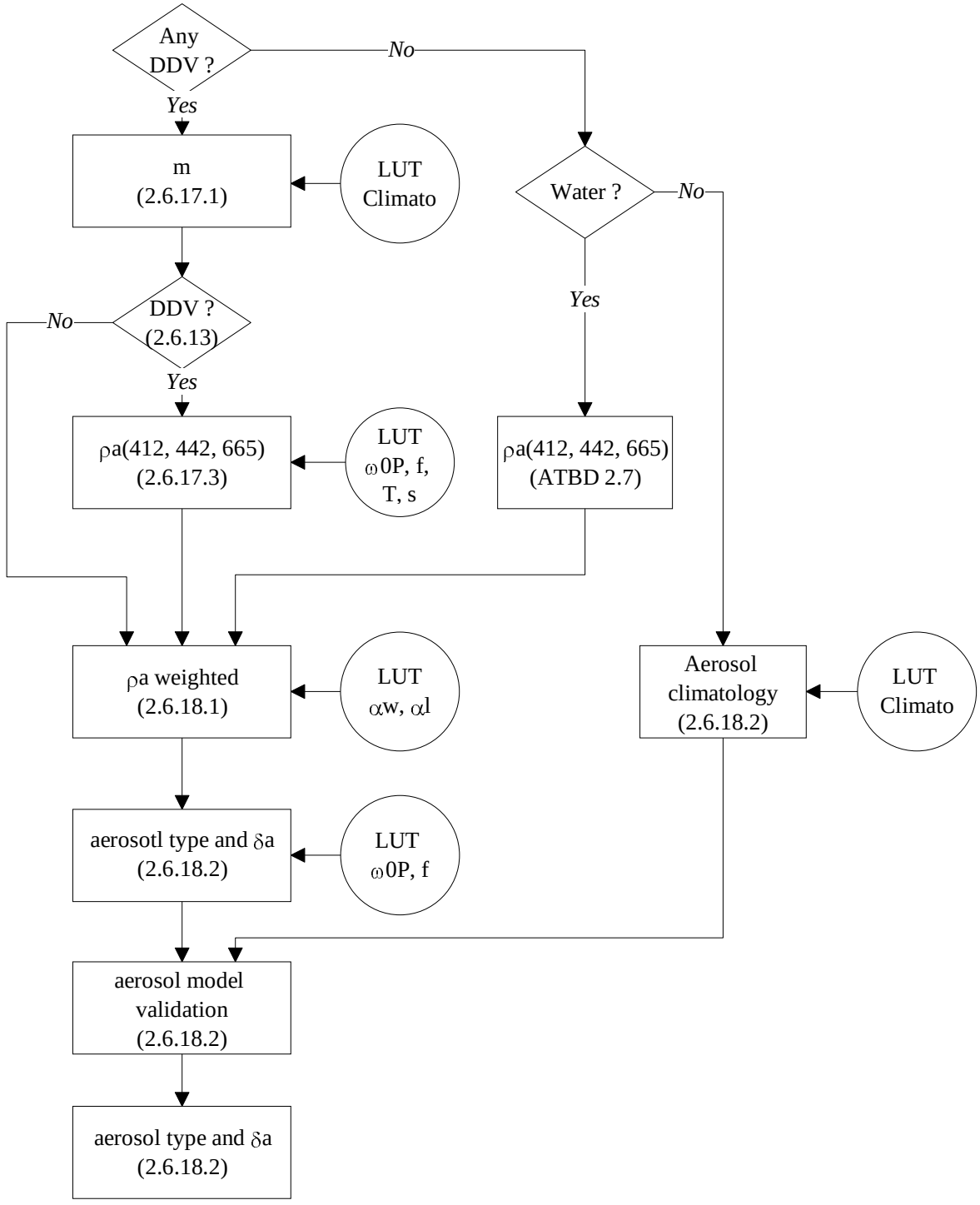

Figure 18: Aerosol model flow chart. (see ATBD 2.19)

If there are enough DDV pixels in the 32*64 window, we obtain the aerosol refractive index (2.6.17.1) from the climatology. If not, before moving to the aerosol climatology (2.6.18.2), we test if there are water pixels in the window. If water pixels are present, we obtain the aerosol reflectance in bands 1, 2 and 7 from the ocean branch (see ATBD 2.7). If we have enough DDV pixels, we loop for each of them (2.6.13) to determine also the aerosol reflectance in bands 1, 2 and 7 (2.6.17.4). In 2.6.18.1, before deriving the aerosol reflectances, we apply the cloud heterogeneity flag as proposed in the pixel identification ATBD (2.17). The surface pressure determined by MERIS comes from the Rayleigh module. The aerosol reflectances are not computed if the flag is raised. If a pixel is not a DDV pixel, we will also use water if present. Now that we have aerosol reflectances eventually both over land and water, we weight (2.6.18.1) these reflectances to have an average value for the window. After that (2.6.18.2), we can propose an aerosol model derived from the MERIS image.

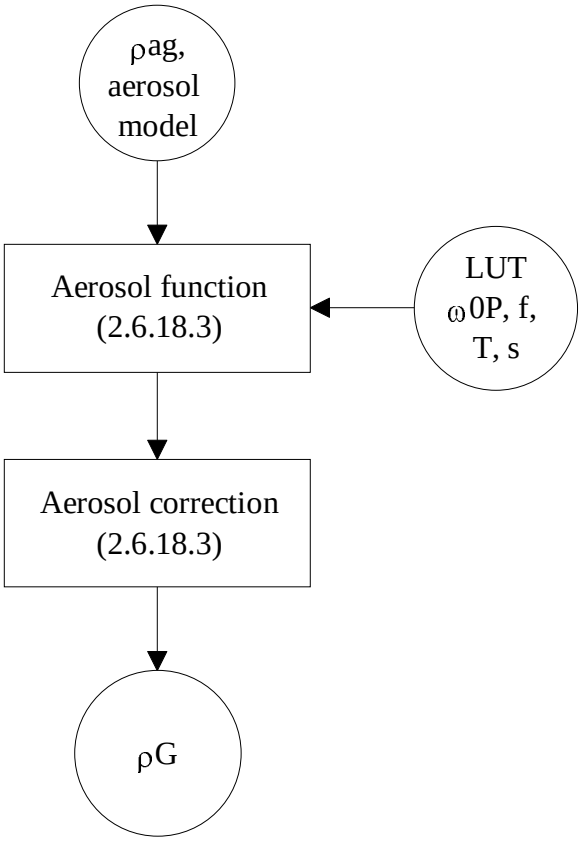

Figure 19: Aerosol correction flow chart.

If the aerosol optical thickness is larger than a threshold, we confirm this model because we can rely more on this determination than on the climatology (2.6.18.2). If not, we have to choose between our aerosol model and the climatology. We have error bars for the remotely sensed aerosol

model on DDV and on water (requirement here from the ocean branch). We also have errors on the climatology in a LUT. We then compare the error on the NDVI for a standard vegetation for the two models. The best aerosol model will be used for the aerosol correction (2.6.18.2).

The top of aerosol reflectances are the inputs to flow chart in Figure 19. The same aerosol model applies to the full 32*64 pixel window and we take the geometry of the 4*4 pixel window to first compute the aerosol scattering functions (2.6.18.3) and then to correct each pixel (2.6.18.3) to provide the surface reflectances.

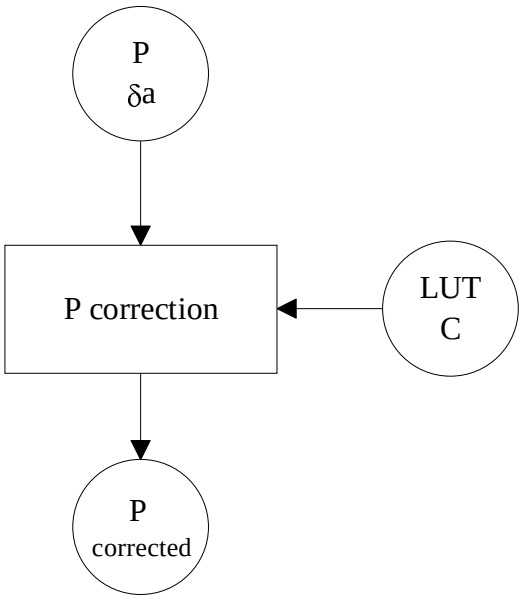

Figure 20: Surface pressure correction flow chart.

Because the surface pressure is a Level 2 product, we refine it in the flow chart of Figure 20 by introducing a corrective factor for the coupling term between scattering and gaseous absorption.

This corrective factor C, which depends on the geometry, can be computed at this stage versus the aerosol optical thickness as well as the surface reflectance.

5. Conclusions and perspectives

A modular atmospheric correction scheme is used based on a simple but robust modeling of the signal with as a starting point the signal decomposition as proposed in 5S. This scheme offers some similarities with the one followed for EOS-MODIS atmospheric correction over land.(Vermote et al., 1997). This modular architecture may allow to include for example the stratospheric aerosols if a major volcanic eruption occurs during the MERIS life time. Because stratospheric aerosols can be described quite simply from auxiliary sources (mainly satellite occultation measurements), they may be precomputed for a reduced number of models (2?) and for few classes of optical thicknesses (5?) and LUTs can be implemented in the Rayleigh module. The main originality of this work lies in the use of MERIS bands in which we have strong gaseous absorptions. We have demonstrated that we can directly correct for the water vapour or oxygen with a simple two band ratio technique when required in a MERIS band. This method, by removing most of the coupling between scattering and absorption, offers a better accuracy as compared to a direct computation of the gaseous transmittances based on calculations for a proposed gas content.

A calibration and validation document is in progress which will address the issues of error budget and algorithm validation.

We plan to first apply and test our algorithm on simulated MERIS images. Simulated MERIS data (13 MERIS channels corresponding to the channels not affected by gaseous absorptions) will be generated using AVHRR data as a support for spatial distribution of the various classes of surfaces and atmospheres. NDVI will be used to assign surface classes including different types of DDV. The AVHRR thermal channel(s) will be used to obtain a different spatial distribution for selected aerosol models (basically the WMO-WCP models which are mixtures of four basic components) and types of clouds. Surface and atmosphere images will then be "recombined" using exact computation of a transfer code (successive orders of scattering), combined with 6S for gaseous transmittance computations, to create the MERIS-like images. The method used to generate the images is obviously different from the inversion algorithm mentioned above. We will apply the algorithm inversion to the simulated images to see if we retrieve what we put in or not and to what accuracy. An error analysis can be conducted on an extensive basis to separate the possible biases generated by the different approximations we used from more statistical errors.

The Rayleigh correction is based on determination of the surface pressure with the O_2 band. We need to validate this technique as well as the associated error analysis. A good candidate for that can be MOS if we have access to the data or any airborne spectrometer as long as we can

reconstruct the necessary MERIS bands. For the aerosol remote sensing, the field of activities is quite large. We first need to identify and characterize DDV. Because POLDER uses the required bands both for ARVI and for aerosol remote sensing, we will use these data starting early 1997. One possible limitation is POLDER spatial resolution (4 x 5 km) but we can certainly use these data over large tropical, equatorial or boreal forests with a possible characterization of these targets under clear atmospheric conditions. Then, under more turbid circumstances, we could apply an inversion scheme to extract the aerosols. A validation of the aerosol remote sensing can be conducted using the POLDER aerosol product based on an independent retrieval using the polarization. Some other aerosol retrievals over DDV using ARVI can be done on existing SPOT (using in fact NDVI for SPOT since the blue channel does not exist) and TM data where concurrent atmospheric measurements exists.

Finally, we plan to fully validate the surface reflectance retrieval scheme presented here through specific campaigns over well-defined test sites, although the correction of surface reflectance for aerosols is deferred to Level 3 processing. These test sites need to offer a large diversity of surfaces as well as a patchy landscape to evaluate the impacts of the environment.

6. References

Bréon F.M. and Bouffiès S., 1996, Land surface pressure estimate from measurements in the oxygen A absorption band, *to be published in Journal of Applied Meteorology.*

Clough S.A., M.J. Iacono, and J.L. Moncet, 1992, Line by line calculations of atmospheric fluxes and cooling rates: application to water vapour, *J.G.R., D, 97, 15761-15785, 1992.*

Deuzé J.L., Herman M. and Santer R. , 1989, Fourier series expansion of the transfer equation in the atmosphere ocean system, *J. Quant. Spectr. Rad. Transfer, 41, 483-495.*

Dubuisson P., J.C. Buriez and Y. Fouquart, 1996, High spectral resolution solar radiative transfer in absorbing and scattering media: application to the satellite simulations, *J. Quant. Spectrosc. Radiat. Transfer, 55, pp 103-126.*

Fischer F., and H. Grassl, 1991, Detection of cloud top height from backscattered radiances within the oxygen A band. Part I: theoretical study, *J. App. Met., 30, 1245-1259.*

Kaufman Y.J. and C. Sendra, 1988, Algorithm for automatic corrections to visible and near-infrared satellite imagery, *Int. J. of Remote Sens., Vol. 9, No 8, 1357-1381.*

Lacis A., and V. Oinas, 1991, A description of the correlated k-distribution method for modeling non-gray gaseous absorption, thermal emission and multiple scattering in vertically inhomogeneous atmospheres, *J. Geophys. Res., 96, 9027-9074*.

Mitchell, R.M. and D.M. O'Brien, 1987, Error estimates for passive satellite measurements of surface pressure using absorption in the A band of oxygen, *J. App. Met., 31, 1179-1192.*

Roger, J.C., Vermote E.F., and El Saleous N., 1994, Atmospheric corrections of MAS data during SCAR-A experiment, *in Proceeding of the European Symposium on Satellite Remote Sensing, Vol. 2311, Rome, Italy, 26-30 September 1994.*

Rothman et al., 1992, The HITRAN molecular database: edition of 1991 and 1992., *J. Quant. Spectrosc. Radiat. Transfer, 48, pp 469-507*.

Scott, N.A., 1974, A direct method of computation of the transmittance function of an inhomogeneous gaseous medium - I: description of the method, *J. Quant. Spectrosc. Radiat. Transfer, 14, 691-704.*

Stamnes K., S.C. Tsay, W. Wiscombe and K. Jayaweera, 1988, Numerically stable algorithm for discrete ordinate method radiative transfer in multiple scattering and emitting layered media, *Applied Optics, 12, 2502-2509*.

Vermote E. and Tanré D., 1992 - Analytical expressions for radiative properties of planar Rayleigh scattering media, including polarization contributions. *J. Quant. Spectrosc. Radiat. Transfer, vol. 47, N^{0}. 4, pp. 305-314.*

Vermote E.F., El Saleous N., and Roger J.C., 1994, Operational atmospheric correction of AVHRR visible and near infrared data, *in Proceeding of the European Symposium on Satellite Remote Sensing, Vol. 2311, Rome, Italy, 26-30 September 1994.*

Vermote E., Tanré D., Deuzé, Herman M. and Morcrette J.J., 1995, Second Simulation of the Satellite Signal in the Solar Spectrum (6S), *User's guide*.

Vermote E., El Saleous N., Justice C.O., Kaufman Y.J., Privette J.L., Remer L., Roger J.C. and Tanré D., 1997, Atmospheric correction of visible to middle-infrared EOS-MODIS data over land surfaces: Background, operational algorithm and validation, *J.G.R., vol, 102, D14, 17131-17141.*

ANNEX: paper in press, International Journal of Remote Sensing

Atmospheric correction over land for MERIS

R. SANTER, V. CARRERE, P. DUBUISSON, and J.C. ROGER

PAMOC, Laboratoire d'Optique Atmosphérique

Université du Littoral

Station Marine de Wimereux, BP 80, 62930 Wimereux, France

Abstract. A three stage atmospheric correction is proposed for MERIS from a validated formulation of the signal. We correct first for the gaseous transmittance. Assuming the ozone correction is well defined, we first illustrate the need to include correction for water vapour continuum which covers most of the MERIS bands. The water vapour transmittance can be computed from the water vapour content obtained by a two band ratio at 900 nm and 890 nm. We demonstrate that a direct association between the transmittance in a given band and the two band ratio is more accurate because of the removal of the coupling between absorption and scattering. Secondly the Rayleigh correction depends on the barometric pressure determined here from a two band ratio method with the oxygen A band. A good accuracy is obtained for the pressure when accounting for the coupling between scattering and gas absorption which mostly depends on the surface reflectance. The Rayleigh reflectance is computed from a Fourier series decomposition in which the primary scattering is corrected for the multiple scattering by a multiplicative factor which is derived from a polynomial regression versus the optical thickness. A similar formulation of the signal is proposed for the aerosol reflectances from 12 pre-defined aerosol models. The aerosol correction relies on a characterization of the aerosol over Dense Dark Vegetation for which an identification criteria is proposed as well as standard reflectance values in the blue and in the red.

1. Introduction

For space observations in the solar spectrum, the presence of the atmosphere substantially modifies the intrinsic contribution of the surface to the signal (in other words the surface reflectance as measured from the ground). Both gaseous absorption, and molecular or aerosol scattering reduce the available downward irradiance at ground level as well as the reflected radiance in the upward path to the sensor. To some extent, the reduction of the surface contribution by the atmosphere can be counterbalanced by the intrinsic atmospheric radiance. For ocean colour activities, because of the relative darkness of the water, the obvious role of the atmosphere led to the application of atmospheric corrections mainly on Coastal Zone Conical Scanner (CZCS) images (Gordon, 1978). For land observations, atmospheric correction was generally neglected up to the recent past mainly because of (i) relatively poor calibration of existing broad band sensors such as NOAA Advanced Very High Resolution Radiometer (AVHRR) or LANDSAT Thematic Mapper (TM) and (ii) the fact that the majority of the community was only interested in qualitative analysis of remote sensing data, mostly based on the use of vegetation indices such as Normalized Differential Vegetation Index (NDVI). An increasing interest for the extraction of physical parameters from remote sensing data, for comparison of results from different sensors, obtained over different locations or at different time of year or even produced by physical models led to a more physically based approach relying on radiative transfer instead of empirical methods. The development of radiative transfer codes such as 5S (Simulation of the Satellite Signal in the Solar Spectrum, Tanré et al., 1990) or LOWTRAN 7 (Kneizys et al., 1988) with their followers 6S (Vermote et al., 1995) and MODTRAN (Berk et al., 1989) made easier the understanding of the problem and emphasized the need to develop atmospheric correction schemes. Reliable, accurate recovery of surface reflectance is now required particularly with the development of new sensors with a higher spectral resolution and more bands.

Most atmospheric correction schemes are based on simplified formulations of the signal in order to make the inversion of the Top Of Atmosphere (TOA) radiances easier. Generally, the gaseous absorption is decoupled from the rest. This correction requires integrated values of the gas

contents in the atmospheric column (mainly water vapour and ozone), values generally available at least from the climatology. The Rayleigh correction is well defined and only requires the barometric pressure. The correction for the aerosols is more problematic, first because of their variable nature and abundances, and then because of their weak contribution to the TOA radiances. Of course, this contribution is emphasized over dark surfaces, and the use of so-called Dark Dense Vegetation (DDV) is generally proposed (see for AVHRR, Holben et al., 1992). For time series when available, the contrast reduction on an image may also provide time variability of the aerosol loading (Tanré et al., 1988).

With the new generation of sensors, we can take advantage of a better absolute calibration (required for ocean observations), a better signal-to-noise ratio for narrower bandwidths, a larger number of spectral bands with some of them specifically devoted to the atmosphere and more auxiliary data. Even if the specifications of the land community on the accuracy required for surface reflectance retrieval are generally not clear, we usually need to achieve the best atmospheric correction we can.

A preliminary stage to an atmospheric correction scheme is to have a simple but robust modeling of the signal which allows to simply convert the TOA radiance into surface reflectance. The signal decomposition involves three steps. In a first stage, the gaseous absorption is removed from the signal. The well-known ozone correction is based on European Center for Meteorology and Weather Forecasting (ECMWF) data. For the water vapour absorption, a differential method between 900 and 890 nm is currently proposed to derive the water vapour content. We avoid this retrieval by directly associating the ratio of the radiances at 900 and 890 nm to the water vapour transmittance in any other MERIS band. In doing so, we cancel systematic errors affecting the water vapour absorption such as the coupling between aerosol scattering and gaseous absorption. The same technique is applied for the O_2 transmittance by associating the O_2 transmittance at 760 nm to the ratio 760 / 753.75 nm. Simulations which include the coupling between absorption and scattering indicate that this direct association is more accurate than a computation which involves O_2 or H_2O concentration as inputs.

We then correct for Rayleigh scattering. Computations with the successive orders of scattering code indicated that we can use a schematic vertical structure of the atmosphere with a pure molecular layer above the aerosols and keep a good accuracy. A 5S-like formulation of the signal is applied to convert the TOA radiance into a top of aerosol radiance. We also propose simple and reduced look-up tables (LUTs) to correct Rayleigh primary scattering from multiple scattering and a simple formulation for Rayleigh transmittance.

The Rayleigh contribution depends on the barometric pressure. This pressure is determined using two MERIS bands at 760 and 753.75 nm in a differential method using the O_2 transmittance which only depends on the product of air mass times pressure squared. A simple correction for the coupling between scattering and absorption versus surface reflectance is proposed. This surface pressure retrieval is shown to have a better accuracy as compared to ECMWF data associated to digital map to correct for surface elevation.

The correction for the aerosols is primarily based on standard aerosols models (here the 12 models used for POLarization and Directionality of the Earth Reflectance (POLDER) aerosol remote sensing over land). Then a reference to the aerosol climatology is made to set the refractive index. The remaining, aerosol optical thickness and the slope of the Junge size distribution, are determined from specific observations over Dense Dark Vegetation (DDV).

DDV pixels are detected using a spectral index, the Atmospheric Resistant Vegetation Index, ARVI (Kaufman and Tanré, 1992). Standard values for DDV reflectances at 412, 442 and 665 nm are proposed in order to retrieve the MERIS reflectances by the proper aerosol model. Of course this aerosol retrieval is only possible over DDV pixels which leads to the definition of a MERIS window for which the same aerosol model applies. Within a window, we then need to weight the different information about the aerosol resulting from pure land observations as well as for mixed windows including coastal waters and land. We will also report on the criteria used to make a choice between our aerosol retrieval and a backup based on the aerosol climatology we have to implement.

2. Algorithm overview

2.1. *Objectives*

The first objective is to provide surface reflectances for all of the MERIS bands, except for those which are specifically devoted to the retrieval of gaseous abundance: the two bands for O_2 (at 760 and 765 nm) and the water vapour band at 900 nm. The conversion of the measured radiance into reflectance is only valid for horizontal targets for which we know the incident solar and view zenith angle. This means that for non-flat areas, a pixel by pixel correction is needed based on the knowledge of the terrain slope which is not available at present time on an operational basis.

Because correcting for the aerosol can be questionable, we wish to provide the user with an easy way to retrieve the reflectance above the surface+aerosol system from available attached information. This information can be a starting point to develop spectral indices for land classification. Information required for the algorithm will also be attached as a product: surface pressure, aerosol type and abundance.

2.2. *Principle of atmospheric correction*

The photons which enter the sensor have different origins and a 6S-like signal decomposition is proposed (Vermote et al., 1995) in an attempt to formulate the different contributions in the simplest way:

(i) the absorption by gases,

(ii) the Rayleigh scattering,

(iii) the aerosol scattering,

(iv) the contribution of the surface, which directly depends on its reflectance.

This signal decomposition is primarily applied to the top of atmosphere radiance based on runs of radiative transfer codes. These runs involve each of the specific contributors in order to

model them and so that coupling between two of them becomes more explicit. The formulation of the signal is a simple analytical formula involving each contribution, allowing a straight forward inversion of the signal to retrieve the surface reflectance.

Because the gaseous absorption is quite residual in the MERIS bands to which we apply the atmospheric correction, we can start by describing the conditions necessary to compute the atmospheric diffusion:

(i) The radiation field is described by four components. Because the ellipticity of light vibration for the terrestrial atmosphere-surface system is assumed to be on average equal to zero, we can describe the radiation field by three Stokes parameters only: I, Q, U. It is pointed out that through the multiple scattering, it is necessary to account for the polarization in the computation of the total radiance.

(ii) The phase matrix for the Rayleigh is quite well established if we neglect the asymmetry of the molecules. The Rayleigh phase function is expressed as:

$$P(\Theta) = \frac{3A\left(1 + \cos^2(\Theta)\right)}{4} + B \qquad (01)$$

where A = 0.9587256 and B = 0.0412744 are given in the 6S manual (Vermote et al., 1995) to account for the molecule asymmetry. The scattering angle Θ is expressed as:

$$\cos(\Theta) = \sin(\theta_s)\sin(\theta_v)\cos(\varphi) - \mu_s\,\mu_v \qquad (02)$$

where subscripts s and v stand for solar and view, θ is the zenith angle, φ the difference in azimuth (with φ = 180 in the backscattering region according to the Successive Order of Scattering convention, SOS, see Deuzé et al., 1989), and μ is the cosine of the zenith angle. The Rayleigh optical thickness versus wavelength is known at a standard pressure of 1013 hPa. This optical thickness is proportional to the barometric pressure at the surface.

(iii) The aerosols are assumed to be spherical to apply the Mie theory. Moreover, one aerosol model corresponds to a single component (same equivalent refractive index) for the whole size spectrum.

(iv) Except during strong volcanic aerosol contamination, aerosols are mainly located in the lower troposphere while most of the molecules are above the aerosol layer. Then a simple description for the vertical distribution of the optical thickness δ is given by:

$$\delta(z) = \delta(0)\, e^{-z/H} \qquad (03)$$

where the scale height H is 2 km for the aerosols. The same schematic distribution is used for the Rayleigh but with H = 8 km. Only one aerosol model is considered for the whole atmospheric column.

(v) The spectral response function of the MERIS bands is accounted for in the computations of the basic Rayleigh optical thickness.

General information on MERIS is given in Table 1. Most of the MERIS bands have to be corrected for ozone absorption. The water vapour continuum has a significant contribution except in the blue. For oxygen, only the MERIS band for surface observation at 775 nm is slightly affected.

For the surface, the reflection is assumed lambertian and we neglect the influence of the surroundings. Correction for directional effects involves knowledge of the surface Bidirectional Reflectance Distribution Function (BRDF) which is not accessible from MERIS data. The introduction of the environment effect is theoretically feasible but will lead to substantial computer time to correct for a second order effect.

The computations will be conducted with the SOS method which solves the transfer equation in a plane parallel atmosphere. Because of the medium size of the MERIS field of view as well as a solar zenith angle limited to 80 degrees, we do not have to account for the Earth sphericity in the computations.

To account for the coupling between absorption and scattering, the MERIS reflectances have been simulated from GAME (Global Atmospheric ModEl), a radiative transfer model developed at the LOA (Laboratoire d'Optique Atmosphérique, Université des Sciences et Technologies de Lille, France) including (1) molecular, aerosols and clouds scattering and (2) H_2O, CO_2, O_3 and O_2 absorption. In this model, the absorption coefficients are obtained from line-by-line calculations (STRANSAC model, Scott, 1974; Dubuisson et al., 1996), using the HITRAN database (Rothman et al., 1992) and with a resolution of 10 cm^{-1} (about 0.5 nm for the O_2 absorption band). Interactions between molecular absorption and scattering are accurately treated using the Discrete Ordinate Method (Stamnes et al., 1988) and the correlated k-distribution method (Lacis and Oinas, 1991). In the case of water vapour absorption, comparisons between GAME and reference calculations have shown differences less than or on the order of 2% in satellite radiances, both for clear or cloudy atmospheres. These reference calculations consist of multiple scattering calculations at each step of a line-by-line model.

2.3. *Signal decomposition*

2.3.1. *Removing gaseous absorption*

Outside of strong absorption bands, the coupling between scattering and gaseous absorption is weak. This assumption leads to express the apparent reflectance ρ^* as :

$$\rho^* \approx \rho^*_{na} T_g \qquad (04)$$

where ρ^*_{na} is the signal ignoring the gaseous absorption and T_g the gaseous transmittance, which can be calculated from simulations. Ozone absorption and scattering processes are decoupled because the O_3 layer is located above the aerosols and mostly above the molecules. This remark can be altered if we have major stratospheric contamination.

For the water vapour, the scale height is roughly the same as the aerosol one. Nevertheless, even in the water band, the coupling term remains weak.

To account for the interactions between scattering and absorbing properties, we define :

$$T_g^c = \frac{\rho^*}{\rho_{na}^*}, \tag{05}$$

instead of simply computing the gaseous transmittance without the scattering effect.

2.3.2. *Modeling Rayleigh scattering*

A schematic model is to consider a two-layer model: molecules over aerosols. An illustration of this approximation is given in the worst case for nadir observations at 412 nm. The continental aerosol model was used with a visibility of 23 km. The results, derived from runs with the SOS method, are plotted in Figure 1 as the relative difference between the actual model and the two-layer one.

We now use the 5S decomposition of the signal:

$$\rho_{na}^* = \rho_R + T_R(\mu_s)\frac{\rho_{aG}}{1 - \rho_{aG} \cdot S_R} T_R(\mu_v) \tag{06}$$

where ρ_{na}^* is the top of atmosphere reflectance, ρ_R the Rayleigh reflectance, ρ_{aG} the aerosol-ground system reflectance, $T_R(\mu_s)$ and $T_R(\mu_v)$ the downward and upward Rayleigh transmittances respectively and S_R the spherical albedo relating to molecules. This expression correctly accounts for scattering processes above the aerosol-ground system with the suitable weight among all of the contributors. The only limitation lies in the assumption that the aerosol-ground system is quite lambertian (Table 2) while in Figure 1, the SOS code fully accounts for the interactions between molecules, aerosols and surface. The directionality of the signal below the molecule layer is mainly due to the aerosols because the surface is assumed to be lambertian. Because atmospheric contribution is high and combined to a generally lower surface reflectance, this modeling is more challenging at short wavelengths.

According to Equation (06), we can easily correct for Rayleigh to get the reflectance above the aerosol+ground system ρ_{aG}^{c} with:

$$\rho_{aG}^{c} = \left(\rho_{na}^{*} - \rho_{R}\right) \frac{1}{T_R\left(\mu_s\right) T_R\left(\mu_v\right)} \tag{07}$$

$$\rho_{aG} = \frac{\rho_{aG}^{c}}{1 + \rho_{aG}^{c} . S_R} \tag{08}$$

Because of the variation of the barometric pressure due to terrain elevation, all Rayleigh scattering functions will be pre-computed as a function of optical thickness instead of for each MERIS band. In order to reduce the dimension of the LUTs related to the Rayleigh reflectance computations, we proposed several simplifications. The idea is (1) to use a Fourier series expansion to cancel the dependency in azimuth φ, (2) to treat the scattering phenomenon as primary scattering corrected by a term due to multiple scattering, and (3) to compute this correction using polynomial regressions.

(1) First, we expand the Rayleigh reflectance for each MERIS band as a Fourier series:

$$\rho_R\left(\mu_V, \mu_S, \varphi\right) = \sum_{s=0}^{2} \left(2 - \delta_{0,s}\right) \rho_R^{(s)}\left(\mu_V, \mu_S\right) \cos s\varphi \tag{09}$$

where $\delta_{0,s}$ is the Dirac Function and where s is the order of the series.

(2) For each term of the Fourier series, $\rho_R^{(0)}, \rho_R^{(1)}, \rho_R^{(2)}$, we correct for the primary scattering $\rho_{R,P}^{(s)}$ also expanded in a Fourier series as for equation (09). The Rayleigh phase function is easily expended into a Fourier series. The primary scattering is proportional to the phase function and to a well known analytical formulation independent in azimuth. We introduce here a multiplicative factor to correct for multiple scattering:

$$f_R^{(s)}(\delta_R) = \frac{\rho_R^{(s)}}{\rho_{R,P}^{(s)}} \tag{10}$$

With the SOS code, these 3 functions $f_R^{(s)}(\delta_R)$ have been computed and fitted. Figure 2 illustrates the smooth behavior of these functions versus the viewing angle and the correct retrieval by a third order polynomial even for this extreme solar zenith angle. In the same way and for a given geometry (Figure 3) the dependence in optical thickness is easily modeled by a second order polynomial fit.

The Rayleigh transmittance $T_R(\mu, \delta_R)$ has been computed using the SOS code and compared with the Vermote and Tanré analytical formula (Vermote and Tanré, 1992):

$$T_R^V(\mu, \delta_R) = \frac{(2/3 + \mu) + (2/3 - \mu)\, e^{-\delta_R/\mu}}{4/3 + \delta_R} \tag{11}$$

This formula has a relative accuracy of 0.1% for transmittance ranging from 1.0 to 0.6, but presents some discrepancies for lower transmittances. For MERIS, the environment allows extreme transmittances of 0.4, which correspond to observations in the blue and a total air mass of 5. Therefore, a polynomial regression of the exact case versus this formula needs to be applied. Figure 4 illustrates this technique. The spherical albedo $S_R(\delta_R)$ will be precomputed for 16 δ_R values, ranging from 0.02 to 0.32.

2.3.3. *Correcting for aerosol scattering*

For the aerosol-ground contribution ρ_{aG} we use the same approach as for the Rayleigh :

$$\rho_{aG} = \rho_a + T_a(\mu_s)\frac{\rho_G}{1 - \rho_G \,.\, S_a} T_a(\mu_v) \tag{12}$$

where ρ_a, T_a and S_a are respectively the intrinsic reflectance, the transmittance and the spherical albedo relative to the aerosols and ρ_G is the surface reflectance.

Using Equation (12), we can deduce the surface reflectance ρ_G from the top of aerosol reflectance:

$$\rho_a^c = (\rho_{aG} - \rho_a) \frac{1}{T_a(\mu_s)\, T_a(\mu_v)} \tag{13}$$

$$\rho_G = \frac{\rho_a^c}{1 + \rho_a^c \,.\, S_a} \tag{14}$$

We will consider the simple description for the size distribution by a power law :

$$n(r) \approx r^{\alpha - 3} \tag{15}$$

where the Angström coefficient α describes the wavelength dependency (λ) of the aerosol optical thickness δ_a:

$$\frac{\delta(\lambda)}{\delta(\lambda')} = \left(\frac{\lambda}{\lambda'}\right)^{\alpha} \tag{16}$$

We are aware that the description by a power law is quite crude and limitative. The main goal here is first to achieve atmospheric correction and then to have a good characterization of the aerosol optical properties through a more or less accurate description of their size distribution and refractive index. The possibility to remotely sense aerosols is, for land observations, very limitative: one can hardly expect to have more than an optical thickness at one wavelength and a spectral coefficient. With a Junge power law, the phase matrix does not depend on wavelength, and the main parameter is the phase function.

For MERIS, we will use 12 aerosol models defined by 4 values of α (0.0, 0.5, 1.0, and 1.5) and 3 values for the real part of the refractive index *m* (1.33, 1.44 and 1.55). These models are close to those proposed for the POLDER ground segment which will probably be used for our aerosol climatology data base. For the 12 aerosol models, we generated the phase functions into LUTs for 83 scattering angles. Thus, for a given aerosol model, we just need to model the dependence in δ_a (we will see in the next section how to determine the model).

The computation of the aerosol reflectance is based on the same idea as for the Rayleigh reflectance e.g. decoupling primary and multiple scattering and use of the Fourier series expansion. But here, we first correct for the primary scattering $\rho_{a,P}$ and only the residual function is expanded into a Fourier series:

$$f_a(\varphi,\delta_a) = \frac{\rho_a(\varphi,\delta_a)}{\rho_{a,P}(\varphi,\delta_a)} = \sum_{s=0}^{n} a_a^{(s)}(\delta_a)\cos(s\varphi) \qquad (17)$$

The Fourier series has been applied to the function f_a in place of the aerosol reflectance ρ_a because f_a is less sensitive to the azimuth φ than ρ_a. Therefore, the order of the series can be reduced. For aerosols, the number of orders of the Fourier series expansion applied to ρ_a can reach 80 (in place of 3 for the Rayleigh). A study for continental aerosols has shown that it was possible to reduce the order of the Fourier series applied to f_a to 6 terms (then n = 5 in Equation (17)) as illustrated in Figure 5. Consequently, we just fitted 6 functions $a_a^{(s)}(\delta_a)$ by a polynomial regression versus aerosol optical thickness. As for Rayleigh multiple scattering correction, a third order polynomial is suitable for aerosol optical thickness δ_a ranging from 0.05 to 1.5. To compute the primary scattering term, we just need the phase function and the single scattering albedo.

The total transmittance T_a, for the direct to direct path, is equal to $T_a(\mu_s).T_a(\mu_v)$. For each aerosol model, for 12 zenith angles, and for 15 values of δ_a, we have LUTs to extract $T_a(\mu)$. The spherical albedo for a given aerosol model is computed versus 15 values of δ_a.

3. Algorithm description

We now have the analytical formulation of the algorithm to transform the TOA reflectances into surface reflectances in a well defined architecture involving three distinct modules. For each module, we will first introduce the required inputs and how we will proceed to perform the corresponding correction. For the remaining, we will suppose that we are dealing with reduced resolution MERIS data (RR mode, 1.2 km). For the full resolution (FR) mode (300 m), if we process pixel by pixel, the same scheme will be applied. If we process a n*n pixel window in the RR mode, then a 4n*4n pixel window will be used in the FR mode.

3.1. *The gaseous correction module*

The gaseous transmittance is the product of the two following transmittances:

(1) ECMWF (or other source) provides the total ozone content in the atmospheric column, U_{O_3}. The total air mass $m = 1/\mu_s + 1/\mu_v$, is computed every 4*4 pixels. The ozone transmittance is defined as:

$$T_{O_3} = e^{\left(-U_{O_3}\, m\, \delta_{O_3}\right)} \qquad (18)$$

with δ_{O_3} as given in Table 1.

(2) To estimate the water vapour transmittance, one possibility is to compute the transmittance from the water vapour content as derived from the ratio 900 nm / 890 nm for which an algorithm exists. Then, if we simply follow the 5S approximation, we just need to correct for the gaseous transmittance in the direct to direct path. However, some uncertainties appear because of the coupling between scattering and absorption, mainly above dark targets and for low atmospheric visibilities. Figure 6 shows that the water vapour transmittance is not well correlated with the two band ratio 900 nm / 890 nm because of multiple scattering effects. Calculations have been performed for various aerosol visibilities (from 50 to 8 km), surface reflectances (vegetation, sand and bare soil

with a constant reflectance of 0.2) and geometrical conditions (solar angles of 30 and 60^o and viewing angles of 0 and 40^o). The surface reflectance is assumed to be the same in the two adjacent bands. The aerosol scattering does not vary significantly as well. The upper envelope is a straight line which occurs when absorption and scattering are almost decoupled for low aerosol loading. This line departs from the first bisector because the residual gaseous transmittance at 890 nm is included in the two band ratio (see Table 1).

Our primary goal is not to obtain U_{H_2O} but only to be able to correct MERIS channels for the H_2O absorption, including the coupling term. Because coupling acts in the same direction in the different bands, we can reduce its influence in a direct relationship between 900 nm / 890 nm and T_g^c at 705 nm. As shown in Figure 7, a good fit by a second order polynomial allows a good retrieval of the transmittance at 705 nm if we measure the ratio 900 nm / 890 nm. This fit is quite accurate regardless of aerosol content and surface reflectance. Here we ran cases for aerosol visibilities ranging from 8 to 50 km, solar angles of 30 and 60^o, viewing angles of 0 and 40^o, tropical, mid-latitude summer and winter atmospheres, and various surface types (same conditions as above).

To simply quantify the gain in accuracy of a direct association between the two band ratio and the water vapour transmittance at 705 nm, let us suppose that we have a water vapour content corresponding to a water vapour transmittance of 0.6 at 900 nm. Depending on the surface reflectance and on the aerosol loading, the two band ratio ranges between 0.64 and 0.76 (see Figure 6). This range gives, according to Figure 7, a water vapour transmittance between 0.86 and 0.93. In comparison, a direct association between the two band ratio and the 705 nm transmittance reduces the error domain to approximately 0.02.

The same technique is applied for each MERIS channel where absorption by water vapour continuum is non negligible, meaning all bands except 490, 442 and 412 nm. We also foresee applying this principle to estimate the O_2 transmittance at 775 nm from the 760 nm / 753.75 nm ratio if necessary. Water vapour and oxygen transmittances are derived for each pixel without geometrical consideration. We are keeping full resolution for water vapour transmittance because the water

vapour content may vary rapidly in time and space. For oxygen, we propose to average on a 4*4 pixel window.

Satellite reflectances ρ^* are then corrected for gaseous absorption T_g assuming Equation (05):

$$\rho^*_{ng} = \frac{\rho^*}{T_g^c} \tag{19}$$

with ρ^* and ρ^*_{ng} measured and corrected reflectances respectively.

3.2. *The Rayleigh correction module*

The Rayleigh optical thicknesses are determined for a surface pressure of 1013 hPa, but in the algorithm we have to take into account the real surface pressure to be accurate. One possibility is to use ECMWF data combined to digital maps. Because of the low spatial resolution of the digital maps (the elevation is provided approximately every 18 km), we prefer here to derive the pressure from the MERIS data themselves.

Several techniques have been used in the past to estimate the cloud top pressure (Fischer and Grassl, 1991) or the surface pressure (Mitchell and O'Brien, 1987; Bréon and Bouffiès, 1996) from measurements in the "A" oxygen absorption band. At this wavelength, the radiation reflected by the surface and measured at the top of the atmosphere is mainly depending on oxygen absorption and therefore on surface elevation.

MERIS carries two channels allowing an estimate of the surface pressure P_s (Figure 8). Assuming no scattering effects in a first approximation, we have calculated with a line-by-line model the ratio R of the reflectance measured in the MERIS oxygen band (760 nm) and in the non-absorbing contiguous channel (753.75 nm) for a large number of geometries (air mass m ranging

from 2 to 6) and surface pressures (ranging from 1050 to 600 hPa). Since we can neglect the small spectral variation of the ground between the two adjacent bands, *R* represents here the gaseous transmittance at 760 nm. Figure 9 shows the ratio *R* as a function of the product $m P_s^2$: the surface pressure is well correlated to the reflectance ratio *R*. This curve can be fitted with a sixth order polynomial and knowing the air mass *m* we have a simple determination of P_S.

However in practice the apparent pressure determined from MERIS measurements can be affected by interactions between absorption and scattering effects. We performed calculations to evaluate the impact of aerosols and molecular scattering on the surface pressure retrieval. The ratio *R* is mainly depending on the surface reflectance ρ_G, solar and viewing geometrical conditions *(*θ_S*,* θ_V*),* the aerosol optical thickness δ_a and the surface pressure P_S.

Surface pressure can be determined from a look-up table, through interpolation according to the ratio R and the previous atmospheric parameter.

This technique has two major inconveniences in the atmospheric correction framework: (1) it requires building a large look-up table covering a realistic variety of atmospheric and geometrical conditions and a large number of interpolations; (2) it requires knowledge of surface reflectance and aerosol optical thickness, implying considerable complications to the atmospheric correction algorithm since these parameters are not known at this stage of the algorithm.

We have then calculated with GAME the ratio *T* between the transmittance in the oxygen band without scattering effects and that accounting for scattering effects. Transmission ratio probability are reported in Figure 10 as a function of the surface reflectance and for aerosol visibilities ranging from 8 to 50 km. Interactions between scattering and absorption are negligible for a transmittance ratio equal to 1. Standard deviations (ΔR^a) and mean transmittance ratios are reported on these curves and show the influence of the surface:

- For bright surfaces, mean transmittance ratio is almost equal to 1. and standard deviation is weak. Neglecting aerosol scattering effects has no dramatic consequences on surface pressure retrieval (error less than 1% on the transmittance ratio).

- For dark surfaces, radiation scattering is no longer negligible but standard deviation remains weak, on the order of a few percent.

The idea is then to retrieve the surface pressure from reflectance ratio calculated without scattering effects (from Figure 9). To take surface effects into account, this reflectance ratio can be modified using a correction factor depending on surface reflectance and the air mass. Since surface reflectance is not known, this correction factor can be determined from apparent reflectances at the top of the atmosphere at 753.75 nm where surface reflectance is the main contributing factor.

Errors ΔR^b originating from using apparent reflectances instead of surface reflectances have been evaluated from simulations with an aerosol visibility of 23 km for the nominal case. Errors ΔR^b presented in Table 3 have been calculated using a visibility of 8 km with continental aerosols. The total error on transmittance ratio ΔR^T is then defined as:

$$\Delta R^T = \sqrt{\left(\Delta R^a\right)^2 + \left(\Delta R^b\right)^2} . \qquad (20)$$

The maximum error is on the order of 1% on the transmittance ratio for a dark surface and of a few tenth of a percent for a bright surface, therefore on the same order of magnitude as the accuracy expected for the calibrated MERIS radiance data. As an example, deviations from the surface pressure have been reported in Table 3 for total air-masses of 2 and 3 and accounting for total error ΔR^T on the corrective factor. In most cases, maximum errors on the surface pressure are less than 25 hPa and can reach 40 hPa for dark surfaces.

Table 3 shows that the method is well adapted to retrieve surface pressure over bright surfaces. Furthermore, the O_2 MERIS channels are located at wavelengths (753.75 and 760 nm) corresponding to the red edge in the case of vegetation and for which sand or bare soil reflectances are generally larger than 0.1. Therefore, the situation will be favorable in most cases. A 4*4 pixel window averaging is then foreseen for the barometric pressure introducing a weighting technique to emphasize the contribution of bright pixels which offers a better accuracy. Of course, in some

mountainous regions, the pressure variations will be important but in these cases it seems difficult to define a surface reflectance because of terrain slopes. The averaged pressure is used to weight in proportion the optical thicknesses reported in Table 1. The Rayleigh atmospheric functions are computed for the mean geometrical conditions over the window. The Rayleigh correction follows Equations (06) and (07).

3.3. *The aerosol remote sensing and correction*

To compute the aerosol functions, we assumed the knowledge of the aerosol properties, but the question is: how to get these properties? In fact, we thought about two possibilities which are usually adopted by the community. The first one consists in retrieving the aerosol optical properties from the data themselves (as described by Kaufman et al., 1996, for example), and the second one, when the former is not possible, is the use of an existing aerosol climatology. For the time being, the climatology is not precisely defined but we are thinking about using the POLDER product. In any case, the climatology will be used as a default option.

3.3.1. *Aerosol retrieval over DDV*

The aerosol remote sensing will be performed over Dark Dense Vegetation (DDV) (Kaufman and Sendra, 1988) for which a definition as well as the identification is reported in Santer et al. (1996). Once we identified the DDV surfaces, we can retrieve aerosol properties assuming a standard value for the DDV reflectance at λ = 412, 442 and 665 nm where the spectral reflectance is the lowest. Because different types of DDV are possible, we certainly need to introduce different models but this question is still open. This method for aerosol remote sensing has been proposed and accepted for several projects on atmospheric correction over land, such as for the MODIS or VEGETATION sensors and has been successfully used with data from the AVHRR instrument (Vermote et al., 1994) and the MODIS Airborne Simulator (MAS) (Roger et al., 1994).

For MERIS, the process starts with the selection of a refractive index for the aerosols from the climatology. We have then 4 aerosol models corresponding to 4 Angström coefficients. For each

of them, we can compute the top of aerosol reflectance according to a 6S-like formulation of the signal similar to Equation (12):

$$\rho_{aG} = \rho_a + T_a(\mu_s)\frac{\rho_{DDV}}{1 - \rho_{DDV} . S_a} T_a(\mu_v) \quad (21)$$

The DDV reflectance ρ_{DDV} at 412, 442 and 665 nm is known from a LUT. The atmospheric functions ρ_a, T_a, S_a , for a given aerosol model, depend solely on δ_a. We then loop on δ_a to retrieve the MERIS reflectances after gas and Rayleigh correction. This retrieval is performed for the 4 aerosol models in the 3 MERIS bands. We select the model for which the Angström coefficient is the closest to the one obtained from the δ_a retrieval.

We checked the opportunity for using one constant standard value per wavelength for the DDV reflectances. Using the BOREAS and POLDER data sets, we defined the surface reflectance for λ = 442 and 665 nm as a mean value (respectively 0.016 and 0.030) and an uncertainty value (respectively 0.004 and 0.010). Using the 6S code, we tested the impact of these uncertainties on the aerosol optical thickness retrieval. Results (Figure 11) show that the impact is negligible at λ = 442 nm but appears more critical at λ = 665 nm. This clearly shows that we have to define a simple DDV reflectance model describing the dependency upon the solar and the viewing angle.

3.3.2. *Aerosol climatology*

At present, one climatology can be made available to the project based on the work published by d'Almeida et al. (1991). We simply have to match their models, which correspond to a mixture of several modes, to the 12 models proposed for MERIS. An optical equivalence can be set based on similar Angström coefficient and asymmetry factor. An updated climatology will be proposed by POLDER on ADEOS and will be more directly available because the basic aerosol models are identical. The first use of the climatology is to set a value for the aerosol refractive index as a pre-requisite for aerosol remote sensing over DDV. If the aerosol characterization from the MERIS image fails, the climatology will also be used as a back-up.

3.3.3. *Aerosol correction*

Because of the impossibility to define an aerosol correction on a pixel by pixel basis, we will open a window for which aerosol parameters will be considered as being constant (an averaged value) over the window. The size of the window first depends on the spatial variability of the aerosol which is quite questionable. We can refer to the aerosol product for POLDER (30 km x 30 km) or for MODIS (50 km x 50 km). For the global coverage, 32 pixels along the scan lines correspond to a variation of 3^o for the view zenith angle. A theoretical study with 6S has shown that, along track, the variation of the solar zenith angle is less than 0.4^o inside a grid of 32 x 64 pixels, anywhere in the world. According to the above considerations, we will propose to use an area corresponding to 32 pixels across track and to 64 pixels along track.

If we have a pure land window, we first assume that we need a certain number of DDV pixels to be representative. If we have a mixed window with water and land, we first assume that the ocean branch provided the aerosol reflectances for λ = 412, 442 and 665 nm.

Once the aerosol model is defined for the 32*64 window, we compute the aerosol functions to be used in Equations (13) and (14) to produce the surface reflectances in 13 MERIS bands. The aerosol type and optical thickness at 865 nm are a Level 2 product. By making the aerosol functions available to the user, it is easy through equation (12) to reproduce the top of aerosol reflectance and just rely on the gaseous and Rayleigh corrections. That can be done, mainly if the climatology back up is used, by users who wish to use new spectral indices for land classification which may offer some resistance to the aerosol scattering.

4. Conclusions and perspectives

A modular atmospheric correction scheme is used based on a simple but robust modeling of the signal with as a starting point the signal decomposition as proposed in 5S. The main originality of this work lies in the use of MERIS bands in which we have strong gaseous absorptions. We have demonstrated that we can directly correct for the water vapour or oxygen with a simple two band ratio technique when required in a MERIS band. This method, by removing most of the coupling between scattering and absorption, offers a better accuracy as compared to a direct computation of the gaseous transmittances based on calculations for a proposed gas content.

The Rayleigh correction is based on determination of the surface pressure with the O_2 band. We need to validate this technique as well as the associated error analysis. A good candidate for that can be MOS if we have access to the data or any airborne spectrometer as long as we can reconstruct the necessary MERIS bands. For the aerosol remote sensing, the field of activities is quite large. We first need to identify and characterize DDV. Because POLDER uses the required bands both for ARVI and for aerosol remote sensing, we will use these data starting early 1997. One possible limitation is POLDER spatial resolution (4*5 km) but we can certainly use these data over large tropical, equatorial or boreal forests with a possible characterization of these targets under clear atmospheric conditions. Then, under more turbid circumstances, we could apply an inversion scheme to extract the aerosols. A validation of the aerosol remote sensing can be conducted using the POLDER aerosol product based on an independent retrieval using the polarization. Some other aerosol retrievals over DDV using ARVI can be done on existing SPOT and TM data where concurrent atmospheric measurements exists.

Finally, we plan to fully validate the surface reflectance retrieval scheme presented here through specific campaigns over well-defined test sites. These test sites need to offer a large diversity of surfaces as well as a patchy landscape to evaluate the impacts of the environment.

We also foresee to conduct an extensive error analysis based on the realization of a land simulator for MERIS. A data base for surface reflectances has been collected for all the MERIS bands. Spatial distribution for surface types is based on AVHRR images; the TOA reflectances are

computed using the SOS code with realistic aerosol models. The orbital as well as the instrumental models will be applied.

5. Acknowledgments

The authors would like to thank Véronique Willart-Soufflet, and colleagues at LOA-Lille and at ACRI for fruitful discussions, and David Dessailly, Gregory Santerre and Moncef Ferjani for technical help. This work is supported by ESA.

6. References

BERK, A., BERSTEIN, L. S., and ROBERTSON, D. C., 1989, MODTRAN: a Moderate Resolution Model for LOWTRAN 7, *AFGL-TR-89-0122, Air Force Geophysics Laboratory, Hanscom AFB, MA 01731 (April 1989)*.

BREON, F.M. and BOUFFIES, S., 1996, Land surface pressure estimate from measurements in the oxygen A absorption band, *to be published in Journal of Applied Meteorology.*

D' ALMEIDA, G.A., KOEPKE, P. and SHETTLE, E.P., 1991, *Atmospheric aerosols, Global Climatology and Radiative Characteristics,* A. Deepak Publishing, Hampton, Virginia USA, 561 p.

DEUZE, J.L., HERMAN, M. and SANTER, R., 1989, Fourier series expansion of the transfer equation in the atmosphere ocean system, *J. Quant. Spectr. Rad. Transfer, 41, 483-495.*

DUBUISSON, P., BURIEZ, J.C. and FOUQUART, Y., 1996, High spectral resolution solar radiative transfer in absorbing and scattering media: application to the satellite simulations, *J. Quant. Spectrosc. Radiat. Transfer, 55, pp 103-126.*

FISCHER, F., and GRASSL, H., 1991, Detection of cloud top height from backscattered radiances within the oxygen A band. Part I: theoretical study, *J. App. Met., 30, 1245-1259.*

GORDON, H. R., 1978, Removal of atmospheric effects from satellite imagery of the oceans, *Applied Optics, vol. 147 pp. 1631-1636.*

HOLBEN, B., VERMOTE, E., KAUFMAN, K.Y., TANRE, D. and KALB, V., 1992, Aerosol retrieval over land from AVHRR data. Application for Atmospheric correction, 1992, *IEEE Transactions on Geoscience and Remote Sensing, vol. 30, No 2, pp. 212-22.*

KAUFMAN, Y.J., and SENDRA, C., 1988, Algorithm for automatic corrections to visible and near-infrared satellite imagery, *Int. J. of Remote Sens., Vol. 9, N^o 8, 1357-1381.*

KAUFMAN, Y.J., and TANRE, D., 1992, Atmospherically resistant vegetation index (ARVI) for EOS-MODIS, *IEEE Trans. on Geosci. and Remote Sensing*, Vol. 30, N^{o}2.

KAUFMAN, Y.J., TANRE, D., CHU, A., MATTOO, S., and REMER L.A., 1996, Algorithm for remote sensing of tropospheric aerosol from MODIS, *MODIS Algorithm Theoretical Basis Document, MOD04, August 1996.*

KNEIZYS, F. X., SHETTLE, E.P., ABREU, L.W. , CHETWYND, J. H. , ANDERSON, G. P. , GALLERY, W. O., SHELBY, J. E. A., and CLOUGH, S.A., 1988, *"Users Guide to LOWTRAN". AFGL-TR-88-0177, Air Force Geophysics Laboratory, Hanscom AFB, MA 01731 (August 1988), ADA 206773.*

LACIS, A. and OINAS, V. , 1991, A description of the correlated k-distribution method for modeling non-gray gaseous absorption, thermal emission and multiple scattering in vertically inhomogeneous atmospheres, *J. Geophys. Res., 96, 9027-9074*.

MITCHELL, R.M., and O'BRIEN, D.M., 1987, Error estimates for passive satellite measurements of surface pressure using absorption in the A band of oxygen, *J. App. Met., 31, 1179-1192.*

ROGER, J.C., VERMOTE, E.F., and EL SALEOUS, N., 1994, Atmospheric corrections of MAS data during SCAR-A experiment, *in Proceeding of the European Symposium on Satellite Remote Sensing, Vol. 2311, Rome, Italy, 26-30 September 1994.*

ROTHMAN, L.S., et al., 1992, The HITRAN molecular database: edition of 1991 and 1992, *J. Quant. Spectrosc. Radiat. Transfer, 48, pp 469-507*.

SANTER, R., CARRERE, V., DUBUISSON, P., ROGER, J.C. and DESSAILLY, D., 1996, Algorithm Theoretical Basis Document, MERIS Level 2 Pixel Identification.

SCOTT, N.A., 1974, A direct method of computation of the transmittance function of an inhomogeneous gaseous medium - I: description of the method, *J. Quant. Spectrosc. Radiat. Transfer, 14, 691-704.*

STAMNES K., TSAY, S.C., WISCOMBE, W., and JAYAWEERA, K., 1988, Numerically stable algorithm for discrete ordinate method radiative transfer in multiple scattering and emitting layered media, *Applied Optics, 12, 2502-2509*.

TANRE D., DESCHAMPS, P.Y., and HERMAN, M., 1988, Estimation of Saharan aerosol optical thickness from blurring effects in Thematic Mapper data, *J. Geophys. Res., pp. 15955-15964.*

TANRE, D., DEROO, C., DUHAUT, P., HERMAN, M., MORCRETTE, J.J., PERBOS, J., and DESCHAMPS, P. Y., 1990, Description of a computer code to simulate the satellite signal in the solar spectrum: 5S code, *Int. J. Remote Sensing, vol. 11, pp. 659-668,.*

VERMOTE, E. and TANRE, D., 1992 - Analytical expressions for radiative properties of planar Rayleigh scattering media, including polarization contributions. *J. Quant. Spectrosc. Radiat. Transfer, vol. 47, N°. 4, pp. 305-314.*

VERMOTE, E.F., EL SALEOUS, N., and ROGER, J.C., 1994, Operational atmospheric correction of AVHRR visible and near infrared data, *in Proceeding of the European Symposium on Satellite Remote Sensing, Vol. 2311, Rome, Italy, 26-30 September 1994.*

VERMOTE, E., TANRE, D., HERMAN, M. and MORCRETTE, J.J., 1995, Second simulation of the satellite signal in the solar spectrum: an overview, *accepted to IEEE.*

Band #	center (nm)	δ_{O_3}	δ_R	Absorbers	T_{O_3}	T_{H_2O} line	T_{H_2O} line + cont.	T_{O_2}
1	412.0	0.000	0.320	----	1.	1.	1.	1.
2	442.0	0.003	0.239	O_3	0.998	1.	1.	1.
3	490.0	0.019	0.157	O_3	0.985	1.	1.	1.
4	510.0	0.039	0.133	O_3+H_2O	0.970	0.993	0.987	1.
5	560.0	0.100	0.091	O_3+H_2O^*	0.926	1.	0.992	1.
6	620.0	0.106	0.060	O_3+H_2O^*	0.922	1.	0.988	1.
7	665.0	0.049	0.045	O_3+H_2O	0.963	0.995	0.981	1.
8	681.0	0.034	0.041	O_3+H_2O	0.974	0.998	0.982	1.
9	705.0	0.020	0.036	O_3+H_2O	0.985	0.906	0.888	1.
10	753.75	0.009	0.027	O_3+H_2O^*	0.993	1.	0.978	1.
11	760.0	0.007	0.026	O_3+H_2O^*+O_2	0.994	1.	0.978	0.380
11b	765.0	0.006	0.025	O_3+H_2O^*+O_2	0.996	1.	0.978	0.648
12	775.0	0.000	0.024	H_2O^*+O_2	1.	1.	0.977	0.994
13	865.0	0.000	0.016	H_2O^*	1.	1.	0.970	1.
14	890.0	0.000	0.014	H_2O	1.	0.945	0.911	1.
15	900.0	0.000	0.013	H_2O	1.	0.647	0.601	1.

* only H_2O continuum absorption

Table 1. General information about MERIS: Rayleigh optical thicknesses for a barometric pressure of 1013 hPa, Ozone optical thickness for 1 cm-atm of Ozone, composition of the absorbers in the different bands. For a solar zenith angle of 45 deg. and a nadir view, we also report the gaseous transmittance for the mid-latitude summer model according to GAME and 6S runs.

	V=23 km			V=08 km		
	(1)	(2)	(3)	(1)	(2)	(3)
	λ=412 nm					
θ_s=0°	0.18721	0.08640	0.18579	0.20516	0.10996	0.20388
θ_s=30°	0.18153	0.07614	0.17677	0.19691	0.09455	0.19054
θ_s=60°	0.20138	0.08036	0.19296	0.22143	0.10756	0.21130
	λ=442 nm					
θ_s=0°	0.17012	0.09654	0.16805	0.18687	0.11700	0.18471
θ_s=30°	0.16376	0.08658	0.15981	0.17734	0.10164	0.15981
θ_s=60°	0.18032	0.08927	0.17109	0.18032	0.08927	0.17109
	λ=560 nm					
θ_s=0°	0.15538	0.13091	0.15510	0.16685	0.14331	0.16669
θ_s=30°	0.14789	0.12221	0.14715	0.15450	0.12869	0.15315
θ_s=60°	0.15301	0.12095	0.14912	0.16351	0.13100	0.15812

Table 2. For the continental model, we computed (1) the signal observed at nadir over vegetation in 3 MERIS bands, (2) the same computations but without Rayleigh scattering, and (3) the actual signal correctly retrieved when adding the molecular atmosphere above the ground+aerosol system and using the 5S approximations.

ρ_S	0.05	0.05	0.25	0.25
air mass	2	3	2	3
R	1.024	1.035	1.001	1.006
ΔR^a	0.010	0.016	0.001	0.005
ΔR^b	0.005	0.01	0.001	0.002
ΔR^{Total}	0.011	0.019	0.001	0.005
P_S (hPa)	990	920	1050	1000
ΔP_S (hPa)	25	40	5	15

Table 3. Uncertainties on the surface pressure retrieval using reflectance ratio without scattering effects and correction factors as a function of surface reflectance.

FIGURE CAPTIONS

Figure 1. Relative influence of the aerosol scale height for H = 0.5, 1.0 and 2.0 km by reference to an aerosol layer below the molecules. The computations are performed at 412 nm using the SOS method in which coupling between aerosols and molecules is accounted for.

Figure 2. Correction functions for Rayleigh multiple scattering as a function of view zenith angle for $\theta_s = 73^o$ and $\delta_a = 0.3$; exact computations (dashed lines) are overlapped by a third order polynomial fit (solid lines).

Figure 3. Correction functions for Rayleigh multiple scattering as a function of δ_R for $\theta_s = 62^o$ and $\theta_v = 32^o$; exact computations (dashed lines) are overlapped by a second order polynomial fit (solid lines).

Figure 4. Representation of the total Rayleigh transmittance as a function of the Rayleigh transmittance as defined by Vermote and Tanré, 1992.

Figure 5. Azimuthal dependency of f for m = 1.44, $\nu = -4.5$, $\theta_s = 73^o$, $\theta_v = 32^o$ and $\delta_a = 0.6$; exact computations (dashed lines) are overlapped by a second order polynomial fit (solid lines).

Figure 6. Gaseous transmittance in the 900 nm MERIS band as a function of the ratio 900 nm / 890 nm, calculated without multiple scattering effects and with an aerosol content ranging from 50 to 8 km, for various surface reflectances and geometrical conditions.

Figure 7. Corrected water vapour transmittance in the 705 nm MERIS band as a function of the ratio 900 / 890 nm.

Figure 8. Oxygen transmittance in the two MERIS channels (760 and 753.75 nm) used for the determination of surface pressure. The oxygen transmittances were calculated with a line-by-line model.

Figure 9. Reflectance ratios calculated from a line-by-line model as a function of the product of the air mass m and the square of surface pressure P_S, for a large number of geometries (m ranging from 2 to 6).

Figure 10. Transmittance ratio probability as a function of surface reflectance and air mass for aerosol visibilities ranging from 8 to 50 km. Standard deviations and mean transmittance ratios are presented on the curves.

Figure 11. Example of error analysis for the aerosol optical thickness retrieval assuming a constant value for the surface reflectance of the DDV (0.016 at 442 nm and 0.030 at 665 nm). We assumed an error on the surface reflectance of 0.004 and 0.010 at 442 nm and 665 nm respectively. Computations have been performed with 6S and using POLDER and BOREAS data sets.

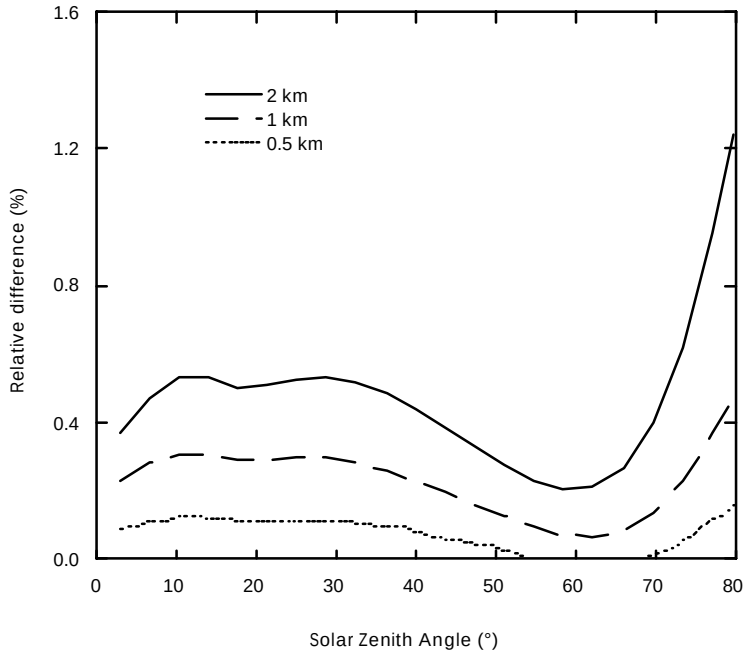
1.6
1.2
0.8
0.4
0.0
Relative difference (%)
2 km
1 km
0.5 km
0
10
20
30
40
50
60
70
80
Solar Zenith Angle (°)

Figure 1

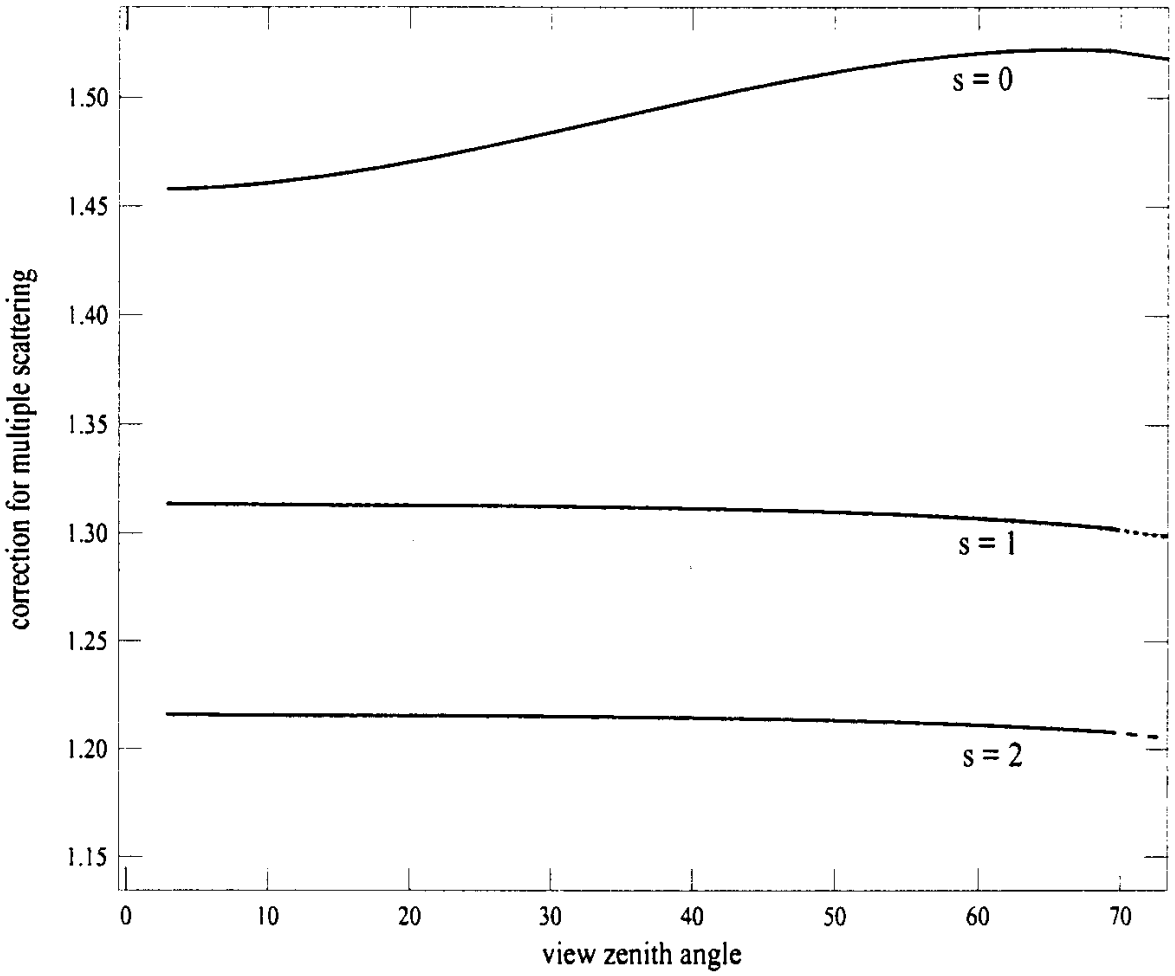
correction for multiple scattering
1.50
1.45
1.40
1.35
1.30
1.25
1.20
1.15
s = 0
s = 1
s = 2
0
10
20
30
40
50
60
70
view zenith angle

Figure 2

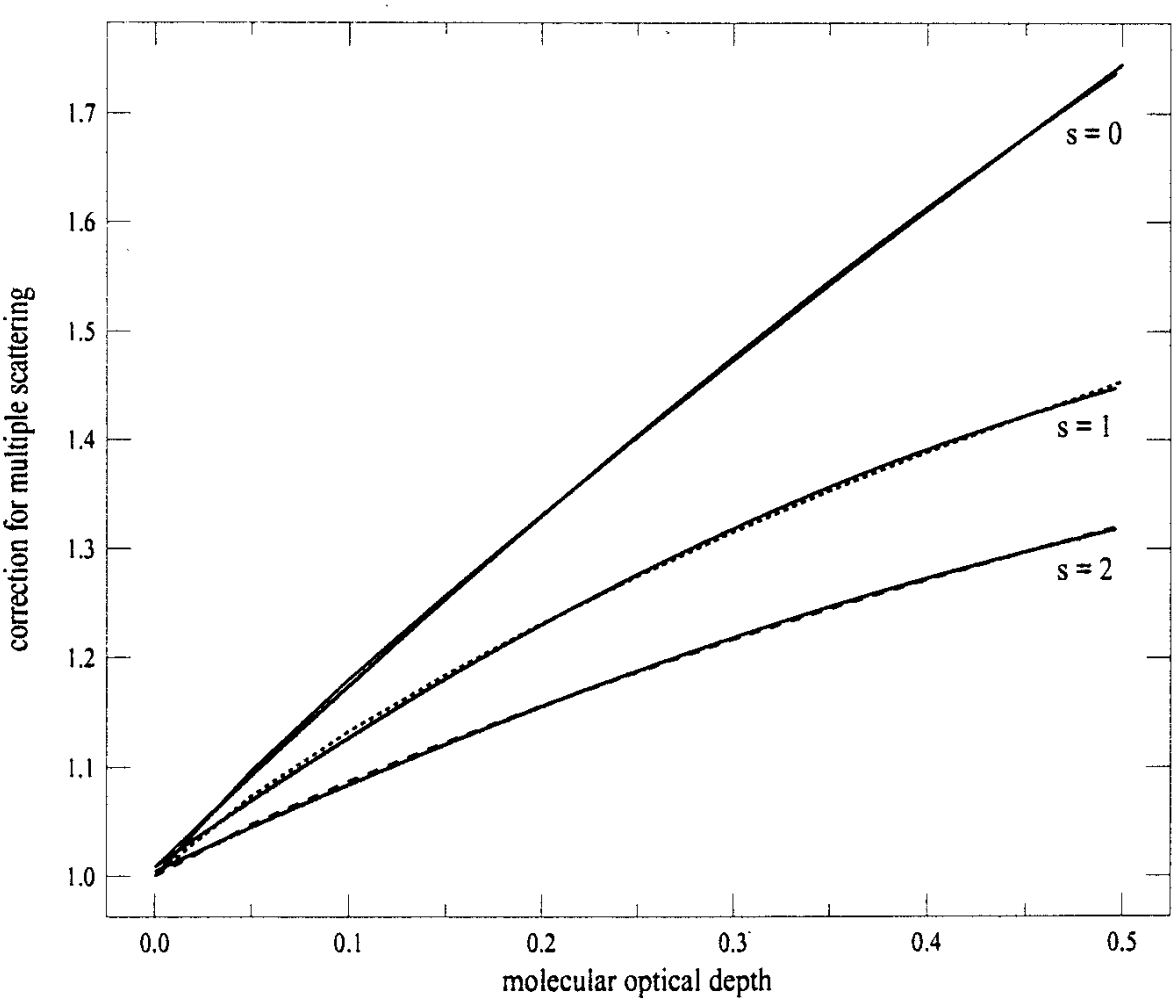
correction for multiple scattering
molecular optical depth
s = 0
s = 1
s = 2
1.0
1.1
1.2
1.3
1.4
1.5
1.6
1.7
0.0
0.1
0.2
0.3
0.4
0.5

Figure 3

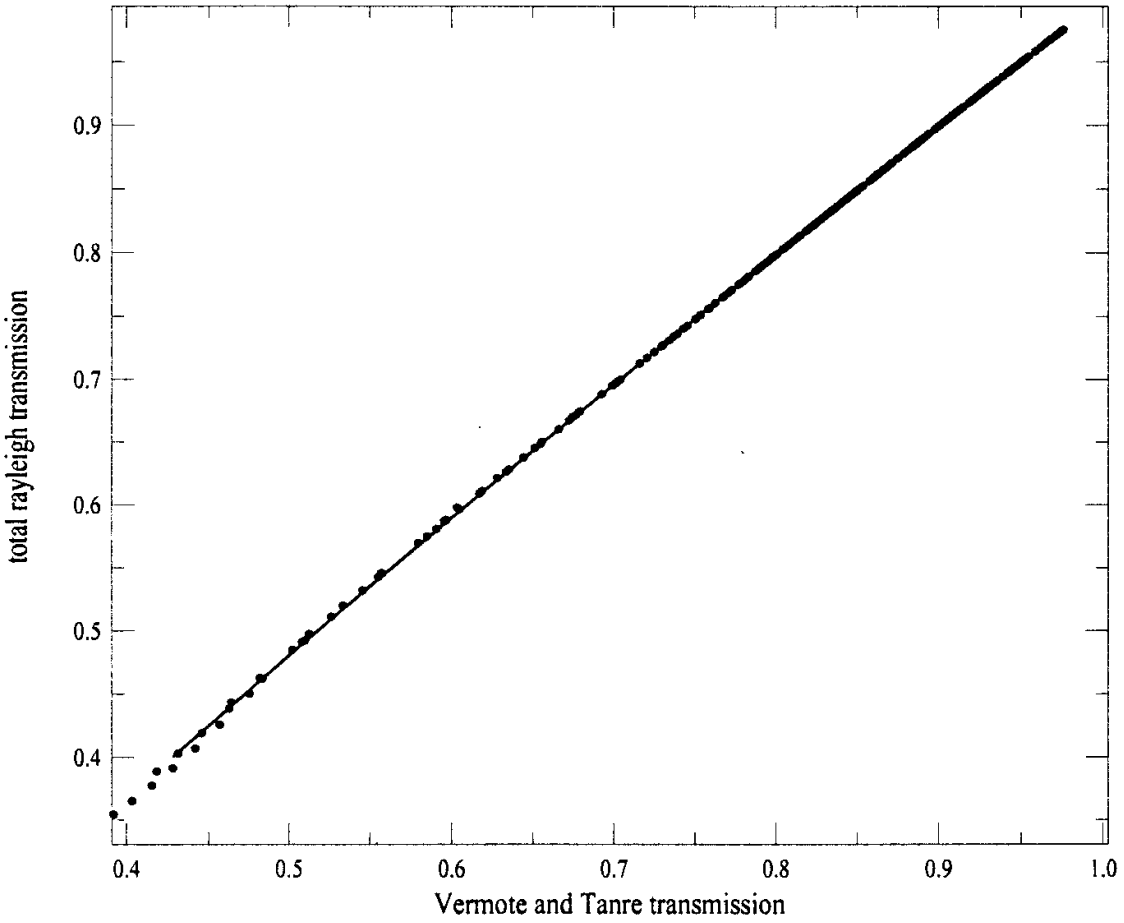
total rayleigh transmission
0.9
0.8
0.7
0.6
0.5
0.4
0.4
0.5
0.6
0.7
0.8
0.9
1.0
Vermote and Tanre transmission

Figure 4

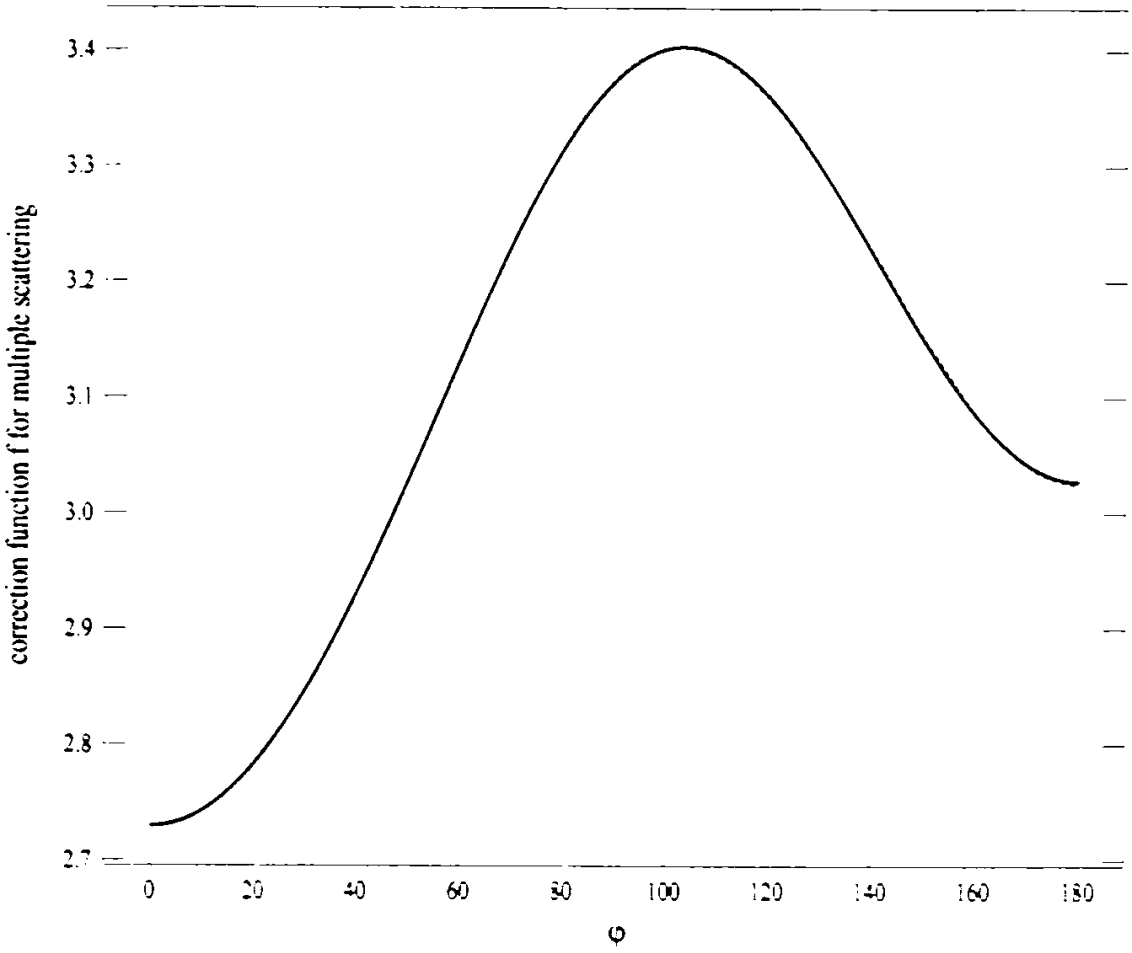
correction function f for multiple scattering
3.4
3.3
3.2
3.1
3.0
2.9
2.8
2.7
0
20
40
60
80
100
120
140
160
180
φ

Figure 5

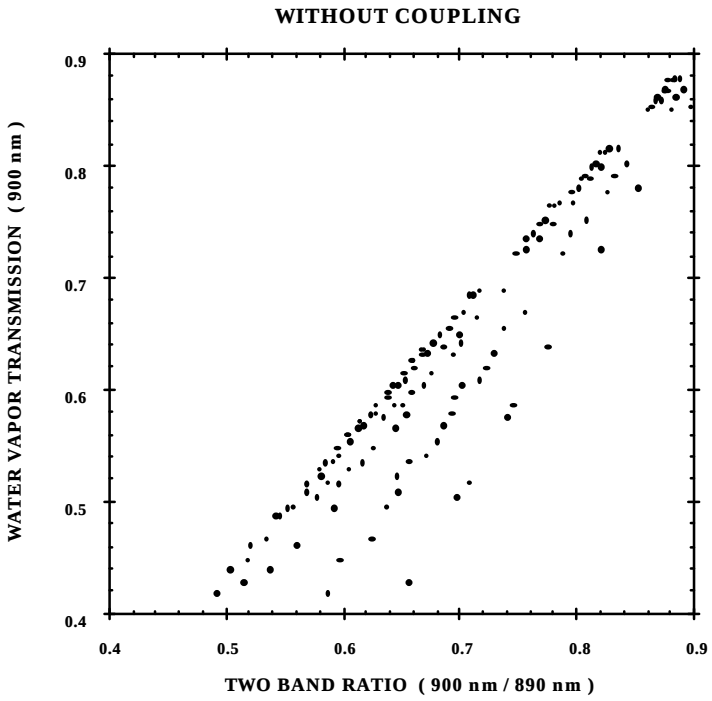
WITHOUT COUPLING
WATER VAPOR TRANSMISSION (900 nm)
TWO BAND RATIO (900 nm / 890 nm)
0.4
0.5
0.6
0.7
0.8
0.9

Figure 6

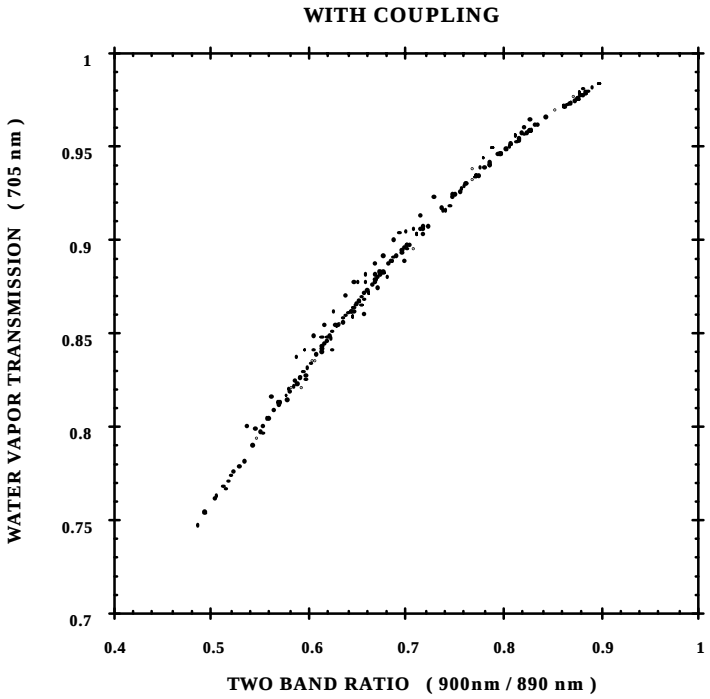
WITH COUPLING
WATER VAPOR TRANSMISSION (705 nm)
1
0.95
0.9
0.85
0.8
0.75
0.7
0.4
0.5
0.6
0.7
0.8
0.9
1
TWO BAND RATIO (900nm / 890 nm)

Figure 7

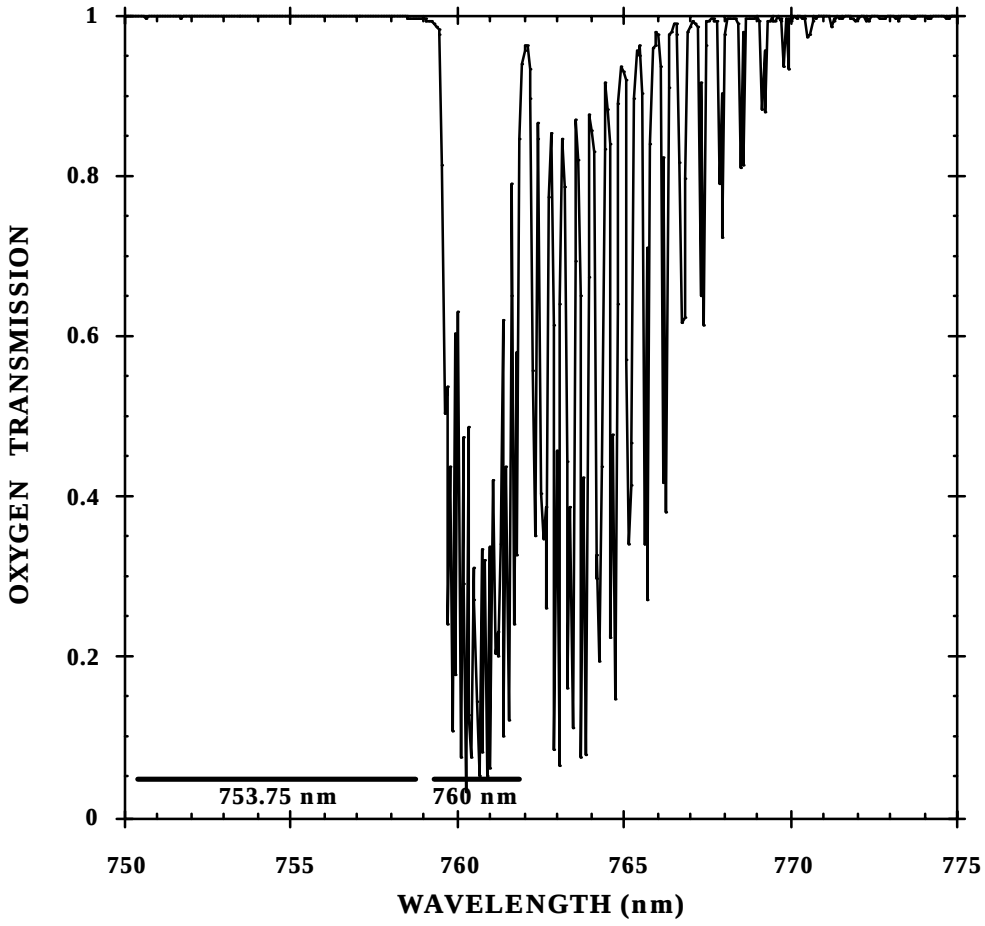
OXYGEN TRANSMISSION
1
0.8
0.6
0.4
0.2
0
753.75 nm
760 nm
750
755
760
765
770
775
WAVELENGTH (nm)

Figure 8

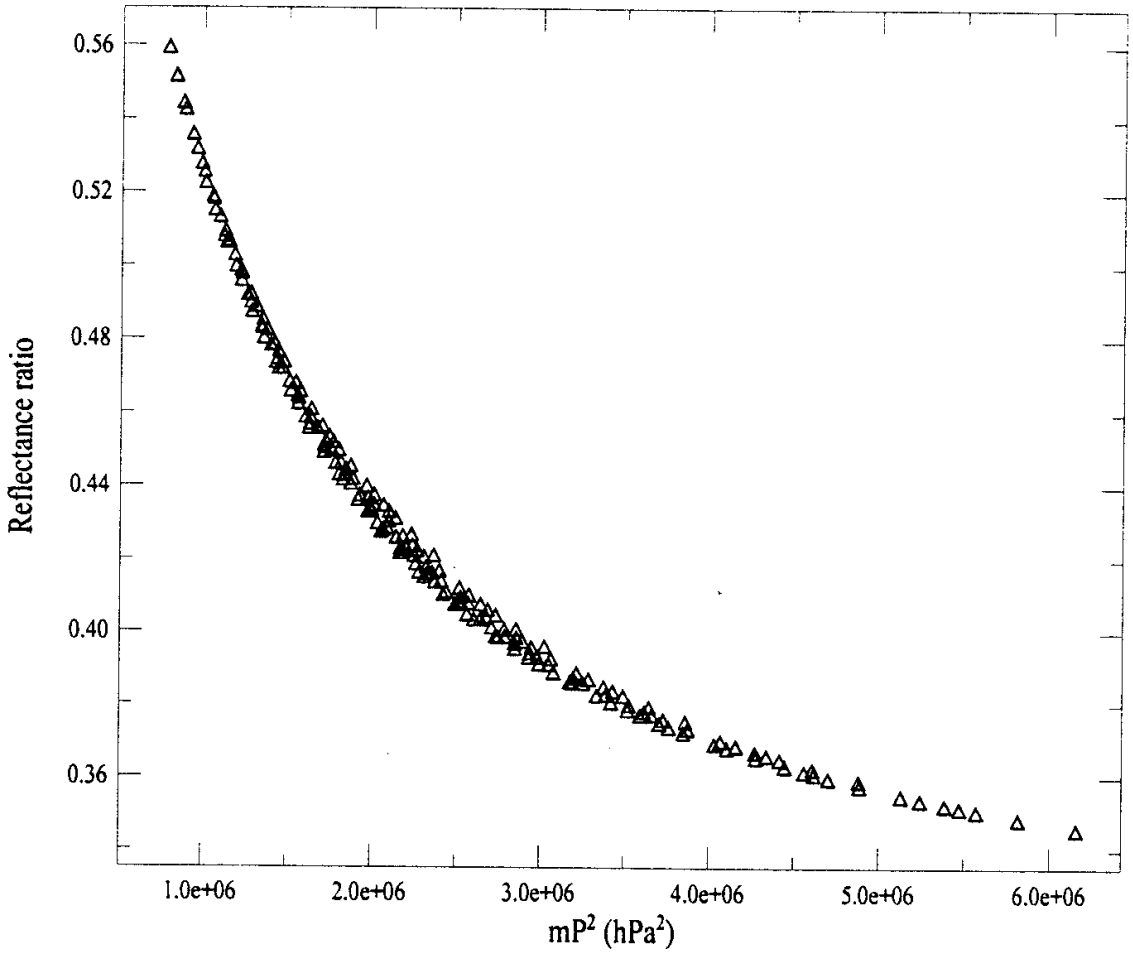
0.56
0.52
0.48
0.44
0.40
0.36
Reflectance ratio
1.0e+06
2.0e+06
3.0e+06
4.0e+06
5.0e+06
6.0e+06
mP² (hPa²)

Figure 9

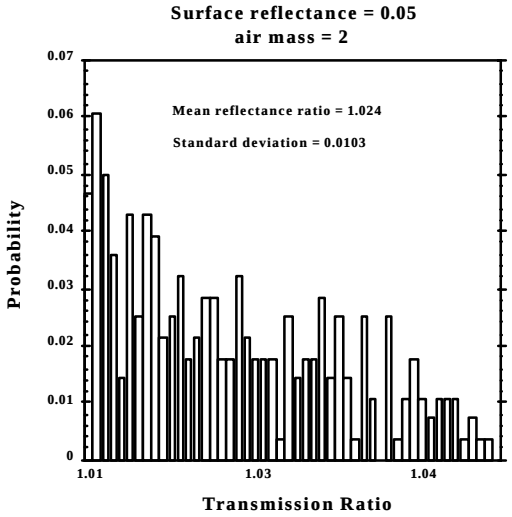
Surface reflectance = 0.05
air mass = 2
Mean reflectance ratio = 1.024
Standard deviation = 0.0103
Probability
Transmission Ratio
0.07
0.06
0.05
0.04
0.03
0.02
0.01
0
1.01
1.03
1.04

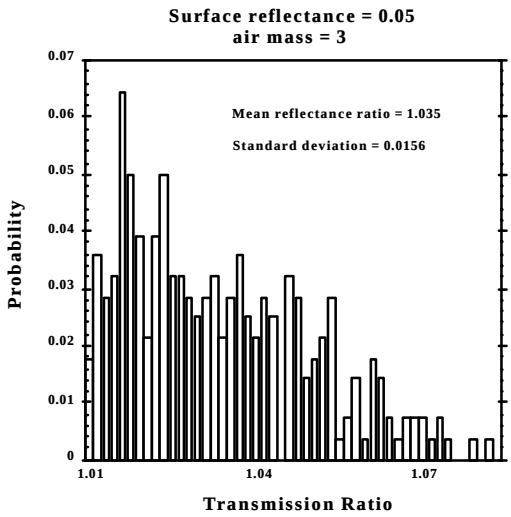
Surface reflectance = 0.05
air mass = 3
Mean reflectance ratio = 1.035
Standard deviation = 0.0156
Probability
Transmission Ratio
0.07
0.06
0.05
0.04
0.03
0.02
0.01
0
1.01
1.04
1.07

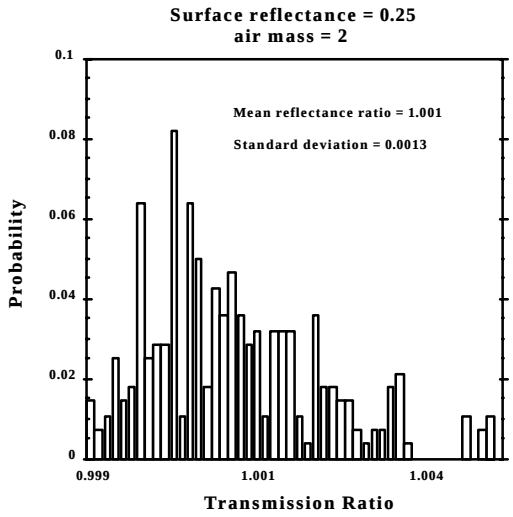
Surface reflectance = 0.25
air mass = 2
Mean reflectance ratio = 1.001
Standard deviation = 0.0013
Probability
Transmission Ratio
0.1
0.08
0.06
0.04
0.02
0
0.999
1.001
1.004

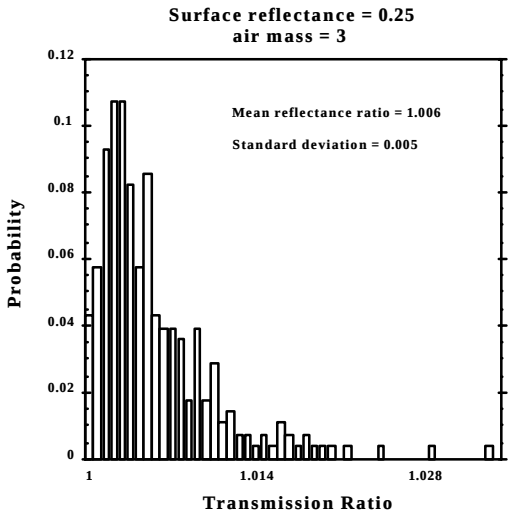
Surface reflectance = 0.25
air mass = 3
Mean reflectance ratio = 1.006
Standard deviation = 0.005
Probability
Transmission Ratio
0.12
0.1
0.08
0.06
0.04
0.02
0
1
1.014
1.028

Figure 10

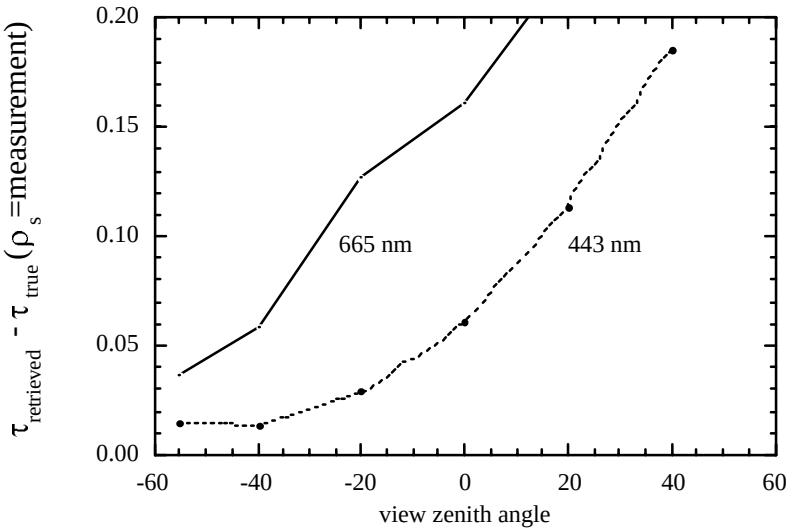
0.20
0.15
0.10
0.05
0.00
-60
-40
-20
0
20
40
60
665 nm
443 nm
view zenith angle
τretrieved - τtrue (ρs =measurement)

Figure 11